ELSEVIER

Journal of Structural Geology 27 (2005) 3–22

JOURNAL OF STRUCTURAL GEOLOGY

www.elsevier.com/locate/jsg

Rounding hinges to fault-bend folding: geometric and kinematic implications

Stefano Tavani*, Fabrizio Storti, Francesco Salvini

Dipartimento di Scienze Geologiche, Università "Roma Tre", Largo S. L. Murialdo 1, I-00146 Rome, Italy

Received 15 January 2004; received in revised form 15 June 2004; accepted 25 July 2004

Abstract

Fault-bend folding is a common folding mechanism in thrust and fold belts worldwide. The widely used kink-band geometric model of fault-bend folding necessitates complex ramp segmentations to reproduce the rounded shape of many natural thrust related anticlines. Curvilinear hinge sectors provide a geometric and kinematic alternative solution to kink bands for modelling curved-hinge folds. We developed an analytical solution for modelling fault-bend folding using circular hinge sectors. The velocity field of this kinematic solution is different from that associated with the classical, kink-style model. Our solution predicts the development of curvilinear anticlines above staircase fault geometries, the occurrence of limb rotation and, consequently, the development of rotational syngrowth wedges on both the forelimb and the crest. Conversely to the kink-style kinematics, curvilinear hinge sectors imply a dependence of deformation intensity from the fold shape and stratigraphic position of the folded layer. Application to natural thrust-related anticlines validates the effectiveness of curvilinear fault-bend folding.

Keywords: Curvilinear fault-bend folding; Geometric model; Circular hinge sector; Limb rotation; Rotational syngrowth wedge

1. Introduction

The shape of natural thrust-related anticlines depends on the interplay among several factors including the mechanical stratigraphy of the folded multilayer (e.g. Corbett et al., 1987; Fischer and Jackson, 1999; Chester, 2003), the folding mechanism (e.g. De Sitter, 1956; Faill, 1973; Ramsay, 1974; Dahlstrom, 1990), the strain rate and state of stress (e.g. Jamison, 1992), the deformation history (e.g. Woodward, 1999), the fault shape (e.g. Rich, 1934; Suppe, 1983; Jamison, 1997; Chester and Chester, 1990), the interaction between tectonic and surface processes, particularly the ratio between fold uplift rate and syntectonic sedimentation rate (e.g. Storti and Salvini, 1996), and rock–fluid interactions (e.g. Morgan and Karig, 1995). Consequently, natural fold shapes range from chevron (e.g. Ramsay, 1974; Fowler and Winsor, 1997) to concentric (e.g. Dahlstrom, 1969). Despite such a variability, the computational simplicity of the kink-style geometry (e.g. Norris, 1961; Faill, 1969; Ramsay, 1974) with respect to curvilinear geometries (Fig. 1) (e.g. Busk, 1929; Price, 1965), determined the adoption of the former fold style in most mathematical models of thrust-related folding (e.g. Suppe, 1983; Jamison, 1997; Chester and Chester, 1990; Mitra, 1990; Suppe and Medwedeff, 1990; Epard and Groshong, 1995; Homza and Wallace, 1995; Poblet and McClay, 1996). In these models, the curvilinear shape of hinge zones is commonly assumed to be a second-order feature suitable to be neglected in the first-order reconstruction of the fold internal architecture (e.g. Woodward et al., 1989). When fold roundness cannot be satisfactorily modelled by a simple kink-band, the fit is improved by increasing the number of constantly dipping panels in the hanging wall (e.g. Suppe, 1983; Jamison and Pope, 1996; Medwedeff and Suppe, 1997). The application of kink-style models to many natural anticlines worldwide supports the geometrical validity of this assumption.

A satisfactory geometrical fit, however, does not necessarily imply that fold kinematics is unequivocally

* Corresponding author. Tel.: +39-654-888049; fax: +39-654-888201
E-mail address: tavani@uniroma3.it (S. Tavani).

0191-8141/$ - see front matter © 2004 Elsevier Ltd. All rights reserved.
doi:10.1016/j.jsg.2004.07.005

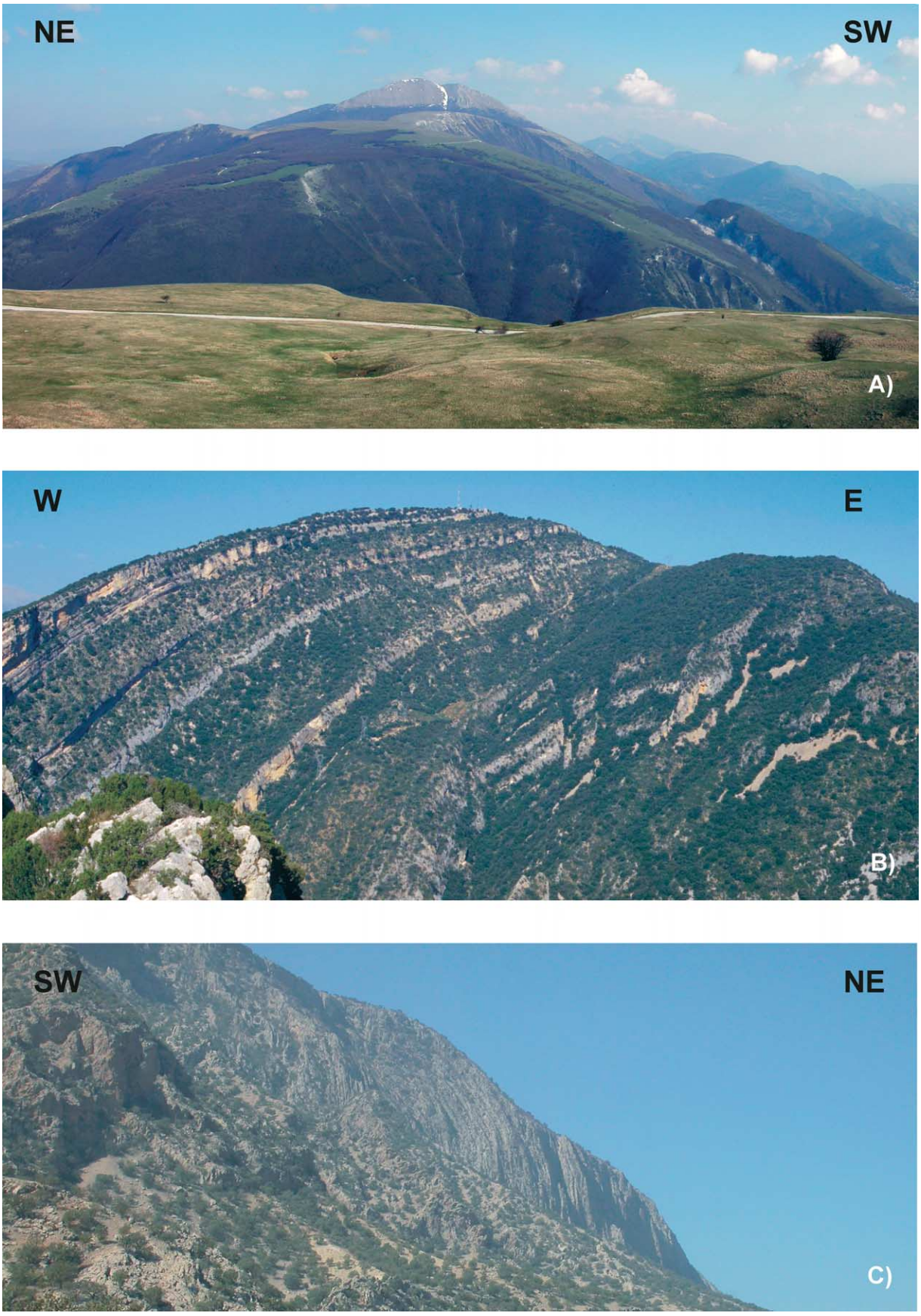

Fig. 1. Examples of curvilinear anticlines: (A) panoramic view of the Mt. Catria Anticline (Northern Apennine, Italy); (B) view of the crest and forelimb of the Mediano anticline (Southern Pyrenees, Spain); (C) panoramic view of the backlimb and its transition to the crest in the Bangestan anticline (Zagros Mountains, Iran).

constrained. Identical fold geometries can be obtained via different kinematic pathways (e.g. Storti and Poblet, 1997). Comparison between a kink-style hinge and a circular sector highlights remarkably different particle paths (Fig. 2a). A kink axial surface imposes an instantaneous transition from the unfolded state to the final attitude of the folded multilayer. The corresponding particle path consists of two straight segments (e.g. Hardy, 1995). On the other hand, a circular hinge sector produces the progressive variation of layer dip up to its final folded attitude. The corresponding particle path is curvilinear. Different particle paths imply (1) different partitioning of layer-parallel slip in flexural-slip folding and (2) different growth stratal geometries when syntectonic sedimentation occurs during folding. (1) With a kink axial surface, the total amount of layer-parallel slip required by parallel folding is instantaneously acquired in the entire folded multilayer (Fig. 2b). Conversely, progressive folding within a circular hinge sector implies the occurrence of infinitesimal increments of layer-parallel slip until the final layer dip is attained. The upward broadening geometry of circular hinge sectors causes a vertically inhomogeneous distribution of layer-parallel slip increments (Fig. 2b). (2) The instantaneous acquisition of final layer dip past a kink axial surface produces growth strata

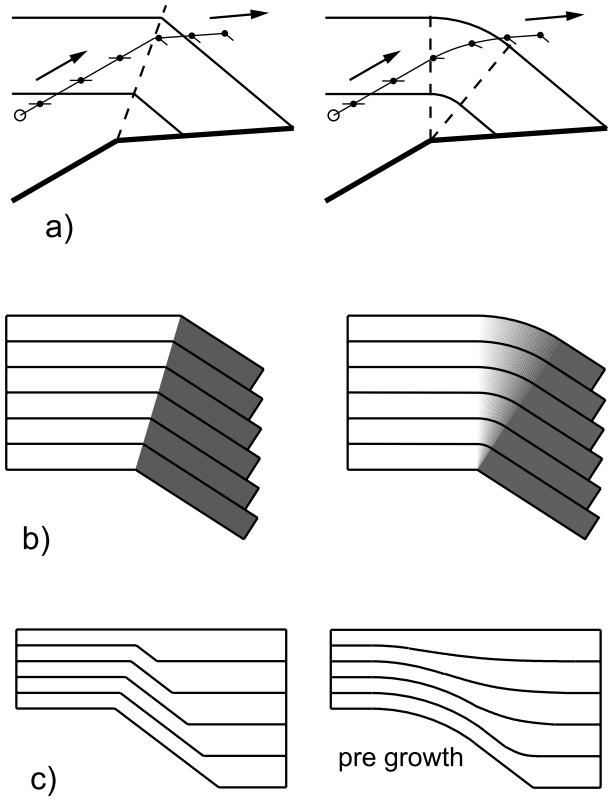

Fig. 2. Comparison between kink-style and circular sector hinges: (a) in the two constructions, motion above the same fault geometry produces different particle trajectories, different fold geometries and different time evolution of bedding dip. The resulting cumulative layer-parallel slip distribution (b), and growth stratal geometries (c), strongly differs in the two hinge styles.

geometries consisting of uniformly dipping rock panels paralleling the top of the pre-growth strata (Suppe et al., 1992). On the other hand, progressive rotation of the substratum during sediment deposition produces wedge-like geometries (e.g. Hardy and Poblet, 1994) (Fig. 2c).

Differences illustrated in Fig. 2 remark how the proper modelling of natural fold geometry cannot be restricted to a mere geometric criterion, suitable to provide multiple solutions. Instead, it includes the choice of the most appropriate fold kinematics, according to the basic milestones of cross-section balancing (e.g. Elliott, 1983). Our major purpose for implementing circular hinge sectors in the classical, kink-style model of Suppe (1983) was to provide an additional kinematic pathway to compressional fault-bend folding (Fig. 3). In our model, parallel folding assumption implies that, when staircase fault trajectories are assumed, anticlinal bends produce circular hinges. On the other hand, synclinal bends produce angular hinges, and curved synclines require curved fault bends. We chose the simplest geometric construction among the wide variety of possible curvilinear hinge sectors and, consequently, our model (in the following referred to as curvilinear fault-bend folding) is an end member of a large class of geometrical solutions suitable to be used in the hinge sectors of fault-bend folds.

2. Circular hinges in fault-bend folding

2.1. Labelling convention

Hanging wall motion above a thrust fault articulated in three straight ramp segments where the central one is the steepest (Fig. 3), produces an anticlinal fold geometry consisting of seven panels named hinterland panel (*HL*), backlimb panel (*BP*), inner circular panel (BP'), crestal panel (*CP*), outer circular panel (FP'), forelimb panel (*FP*) and foreland panel (*FL*). Folding is produced by translation of the hanging wall above the three ramp sectors, respectively named the lower, central and upper ramp.

Adjacent rock panels are separated by straight (γ_1–γ_6) and parabolic (γ_7 and γ_8) hinges (Fig. 4): the shape of the latter is imposed by the adoption of circular sectors and varies with increasing displacement. The across strike length of parabolic hinges depends on the fault shape, on the thickness of the hanging wall, and on the amount of slip (Fig. 4). Hinge γ_1, is pinned at the lower inflection point of the central footwall ramp (I_1) and bisects the angle between *HL* and *BP* panels. Hinge γ_2 is pinned at the stratigraphic elevation (Sc_1) of the central hanging wall ramp lower inflection point (C_1) and is perpendicular to layering in the *BP* panel. For small amounts of displacement (Step I, Fig. 3a), γ_1 and γ_2 join at point C_2 from which hinge γ_7 originates. Hinge γ_3 is pinned at C_1 and hinge γ_4 is pinned at the upper inflection point of the central footwall ramp (I_2), as well as γ_5. The latter is perpendicular to bedding in the

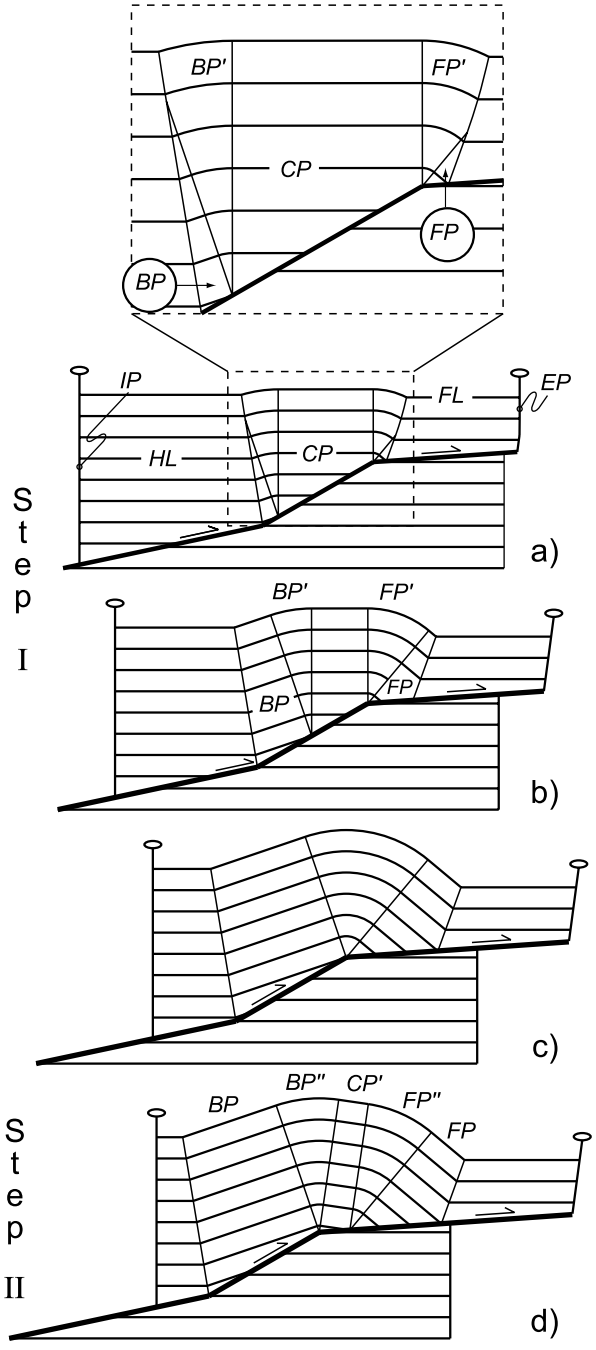

Fig. 3. Geometric and kinematic evolution of a curvilinear fault bend anticline. See text for details.

FP panel. Hinge γ_6 is pinned at the stratigraphic elevation (Sc_3) of the central hanging wall ramp upper inflection point (C_3) and bisects the angle between *FP* and *FL*. Hinges γ_5 and γ_6 joint at point C_4 from which hinge γ_8 originates. When the entire central hanging wall ramp is translated onto the upper footwall ramp (Step II, Fig. 3d), two new straight hinges originate and bound panel CP' (Fig. 4b): γ_3' is pinned at the upper inflection point of the central footwall ramp, while γ_4' is pinned at C_1 and migrates with it (Fig. 4b).

The footwall cut-off angles in the lower, central and upper ramp are named α_1, α_2 and α_3, respectively (Fig. 4a). The hanging wall cut-off angles are α_1 in the *HL* panel, β_1 in the *BP* panel, β_2 in the *CP* panel, β_3 in the *FP* panel and β_4 in the *FL* panel. The inter-hinge angle $\gamma_1\hat{}\gamma_2$ is ϕ_1 and $\gamma_5\hat{}\gamma_6$ is ϕ_2. The angles at the apexes of BP' and FP' are δ_1 and δ_2, respectively. The backlimb, crest, and forelimb dip are η_b, η_c and η_f, respectively. During Step II, the angular parameters are preserved unvaried except for δ_1, δ_2, β_1 and η_c that become δ_1', δ_2', β_1' and η_c', respectively (Fig. 4b). Linear parameters include the amount of slip along the lower (S_1), central (S_2) and upper ramp (S_3), and the length of the central ramp (R).

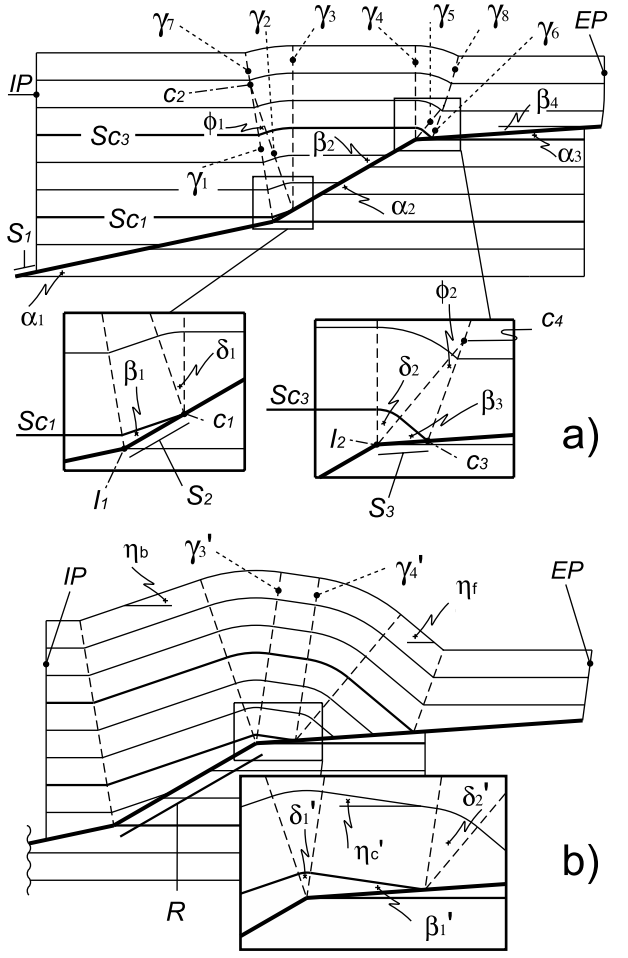

Fig. 4. Labelling convention for the mathematical modelling of curvilinear fault-bend folding. See text for details.

2.2. Fold kinematics

The adoption of circular hinge sectors (e.g. Julivert and Arboleya, 1984; Rafini and Mercier, 2002) to geometrically model fault-bend anticlines (Rich, 1934), produces an overall fold shape resembling that of the kink-style folding. Circular sectors pinned at the fault surface replace straight axial surfaces characterising the backlimb–crest and crest–forelimb transition in the kink-style model (Fig. 5). Pinning

the circular sectors at the fault surface (e.g. Julivert and Arboleya, 1984) is the easiest geometrical and analytical solution and provides a reasonable approximation of natural structures (Fig. 6).

In our model, line-length and bed thickness are preserved and flexural slip folding is assumed (Suppe, 1983). This means that the fault shape and the amount of shortening impose the fold shape. In the early stages of contraction (Step I), the *BP* and *FP* panels and the circular hinge sectors BP' and FP' are still incomplete (Fig. 3a). Material enters from *HL* into the backlimb of the anticline (*BP* and BP' panels) through the active axial surfaces (Suppe et al., 1992) γ_1 and γ_7, respectively. The circular sector FP' and panel *FP*, in the forelimb, grow by the addition of material from the crestal panel *CP* and from the foreland through the active axial surfaces γ_4 and γ_8, respectively. With increasing contraction, the *BP* panel in the backlimb and the *FP* one in the forelimb diachronously develop. The width of *BP*, BP', FP' and *FP* increases, while *CP* narrows (Fig. 3b). The circular sector BP' is passively transported along the central footwall ramp and is fixed because no material passes across it (Suppe et al., 1992). Conversely, the circular sector FP', which is pinned at the central hanging wall ramp upper inflection point, is active. Fold growth induces a forelandward shear in the foreland material and, consequently, the external pin (*EP*) undergoes a limited clockwise rotation. The forelandward shear non-linearly increases with increasing distance from the upper ramp and *EP* has a parabolic shape until points C_2 and C_4 reach the top of the folded multilayer. The upward completion of the *BP* and *FP* panels induces a linear distribution of layer parallel shear in the foreland and *EP* attains a straight trajectory.

When the curvature centre of BP' reaches the upper inflection point of the central footwall ramp, the crestal panel *CP* disappears and the two circular hinge panels merge, forming a wide rounded crestal zone (Fig. 3c). This geometric configuration is a singularity in the evolutionary pathway of the fold. The next step of contraction (Step II) causes the rounded crestal zone to split again into two circular panels (BP'' and FP'') separated by a new crestal panel (CP'). The circular hinge sector BP'' is pinned at the central footwall ramp upper inflection point and is active, while the circular hinge sector FP'' is fixed and is passively transported along the upper footwall ramp. During Step II, FP'', *FP* and *FL* are passively transported along the upper footwall ramp and their shape and size remain unchanged, while panel CP' widens. The ramp geometry of the hanging wall rocks causes the continuous thickness increase in panels CP', BP'' and *BP* (Fig. 3d). When the lower and upper ramps are parallel to layering (simple step; Suppe, 1983), such thickness increase does not occur and only CP' widens (Fig. 7).

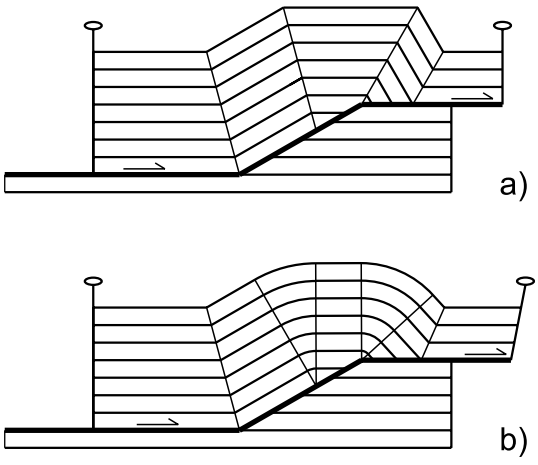

Fig. 5. Comparison between kink-style (a) and curvilinear (b) fault-bend folding. Fault-bend anticlines developed from identical undeformed multilayers, above identical fault shapes and by the same amount of fault displacement.

2.3. Transient stage

Adoption of circular hinge sectors in curvilinear fault-bend folding imposes a transient geometric configuration in the anticlinal crest, forelimb, and foreland panels. During this transient stage, which is dictated by line-length preservation in the early stages of deformation, the stratigraphical elevation of point *C*2 is lower than Sc_3 (Fig. 8a). The hinterlandward side of the crestal panel is characterised by a constant cutoff angle β_2. The forelandward side has a variable cutoff angle, β_2^*, initially equalling α_2 and then progressively lowering, to eventually equal β_2. The two sectors are separated by the active axial surface γ_t paralleling γ_3 and pinned at the stratigraphic elevation of C_2. The upward migration of C_2 causes the forelandward migration of γ_t and the progressive widening of the constant-cutoff sector (Fig. 8b). When the stratigraphic elevation of C_2 reaches the upper inflection point of the central ramp, γ_t coincides with γ_4 and the entire crestal panel has a constant cutoff angle. With increasing contraction, γ_4 remains parallel to γ_3 and γ_t enters the forelimb, becoming parallel to γ_5 and dividing it into a constant and a variable cutoff sector, respectively (Fig. 8c). At this stage, the entire foreland panel has a very gentle hinterlandward dip. When the stratigraphic elevation of C_2 reaches that of C_3, γ_t enters the foreland, the entire forelimb attains a constant cutoff β_3, and the transient stage terminates. Further forelandward migration of γ_t produces a constant cutoff sector (β_4) in the foreland panel, adjacent to the forelimb. This sector progressively widens with increasing displacement (Fig. 8d). At this stage if the stratigraphic elevation of C_2 becomes higher than that of C_4, γ_t becomes pinned at the stratigraphic elevation of the latter.

Occurrence of the transient configuration in the early stage of fold growth does not significantly impact the first-order geometric and kinematic evolution of curvilinear fault-bend anticlines for central ramp cutoff angles lower than 45°. This means that the role of the transient

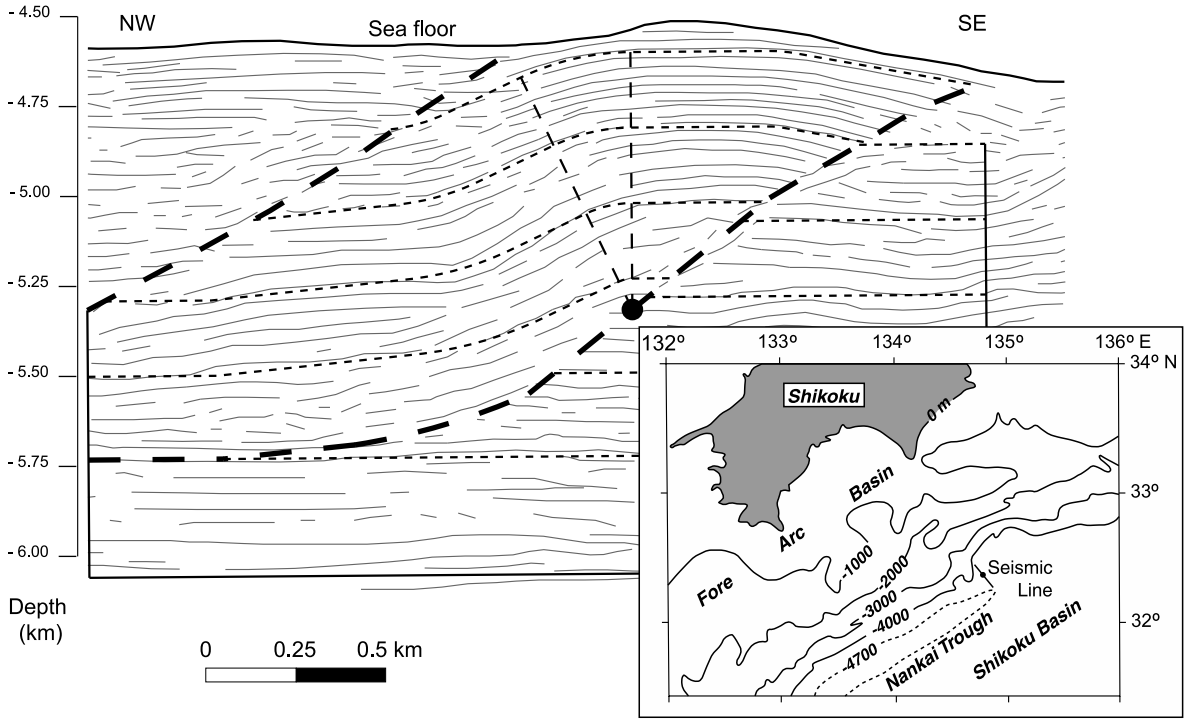

Fig. 6. Application of curvilinear fault-bend folding to a frontal anticline at the toe of the Nankay accretionary prism. The seismic profile shows a well-developed circular hinge sector at the backlimb–crest transition whose curvature centre lies along the fault surface. Line drawing from the original seismic line in Morgan and Karig (1995).

configuration can be neglected for the commonly observed ramp cutoff angles. However, an exact analytical solution of round-shaped fault-bend folding can be easily provided only for constantly dipping panels, i.e. when C_2 is stratigraphically higher than C_3 and the variable cutoff panel is confined to the foreland (Fig. 8d).

2.4. Velocity field

The velocity field associated with curvilinear fault-bend folding predicts that particles have trajectories that are either parallel to the thrust surfaces or curvilinear (Fig. 9). Fold sectors where particle paths are parallel to the fault traces are named *translational sectors*, while parabolic or circular trajectories characterise *rototranslational sectors*. Translational sectors do not include the possibility for particles to modify their distance from the corresponding fault segment. Conversely, particles moving through rototranslational sectors can change their distance from the fault (Fig. 2a). A primary difference between velocity properties characterising translational and rototranslational sectors, respectively, is that layer dip remains constant in the former sectors, whereas it gradually changes in the latter. The velocity field of a curvilinear fault-bend anticline in the post-transient configuration includes one rototranslational sector. In step I (Fig. 10a and b), *HL*, *BP*, *BP′*, *CP*, *FP* and *FL* are translational sectors and *FP′* is the rototranslational sector. In step II (Fig. 10d), *BP″* becomes a rototranslational sector while *FP″* becomes a translational sector.

The presence of rototranslational sectors indicates that limb rotation occurs during the development of round-shaped fault-bend anticlines. In particular, the forelimb rotates in the early stages of folding up to the end of step I (Fig. 10a and b). During step II, the forelimb and the crest become part of a large translational sector (*TS*) and limb rotation is confined to the transition zone between the backlimb and the crest (Fig. 10d).

2.5. Analytical solution

The quantitative description of curvilinear fault-bend folding includes the formalisation of geometrical relations among angular and linear parameters, the mathematical description of the incremental positions of points C_2 and C_4, and of γ_7 and γ_8. Equations describing angular parameters are listed below and their graphical solutions are illustrated in Fig. 11. The complete mathematical description of the model is provided in Appendix A:

$$\phi_1 = (\alpha_2 - \beta_1)/2 \tag{1}$$

$$\eta_b = \alpha_2 - \beta_1 \tag{2}$$

$$\cot(\alpha_1) = \cot(\beta_1) - 2\tan[(\alpha_2 - \beta_1)/2] \tag{9}$$

$$\delta_1 = \beta_2 - \beta_1 \tag{17}$$

$$\cot(\beta_2) + \beta_2 = \cot(\alpha_2) - \cot(\alpha_1) + \cot(\beta_1) + \beta_1 \tag{18}$$

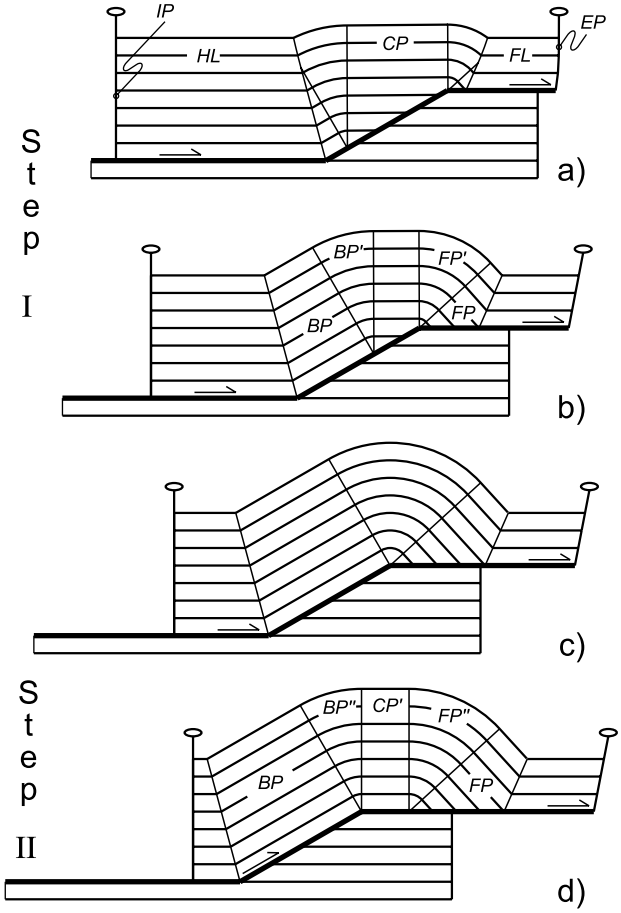

Fig. 7. Geometrical and kinematic evolution of a curvilinear fault-bend anticline developing above a thrust whose lower and upper ramps are parallel to layering (simple step model). See text for details.

$$\eta_c = \alpha_2 - \beta_2 \tag{19}$$

$$\delta_2 = \beta_3 - \beta_2 + \alpha_2 - \alpha_3 \tag{25a}$$

$$\delta_1' = \beta_1' - \beta_1 + \alpha_2 - \alpha_3 \tag{25b}$$

$$\cot(\beta_3) + \beta_3 = \alpha_3 - \alpha_2 + \cot(\beta_2) + \beta_2 \tag{26a}$$

$$\cot(\beta_1') + \beta_1' = \alpha_3 - \alpha_2 + \cot(\beta_1) + \beta_1 \tag{26b}$$

$$\phi_2 = (\beta_3 - \beta_4)/2 \tag{28}$$

$$\cot(\beta_4) - 2\tan[(\beta_3 - \beta_4)/2] = \cot(\alpha_3) - \cot(\alpha_2) + \cot(\beta_3) \tag{41}$$

$$\eta_c' = \beta_1' - \alpha_3 \tag{42}$$

$$\eta_f = \beta_3 - \alpha_3 \tag{43}$$

$$\delta_2' = \beta_3 - \beta_1' \tag{45}$$

These equations allow construction of the shape of a curvilinear fault-bend anticline in the post transient stage.

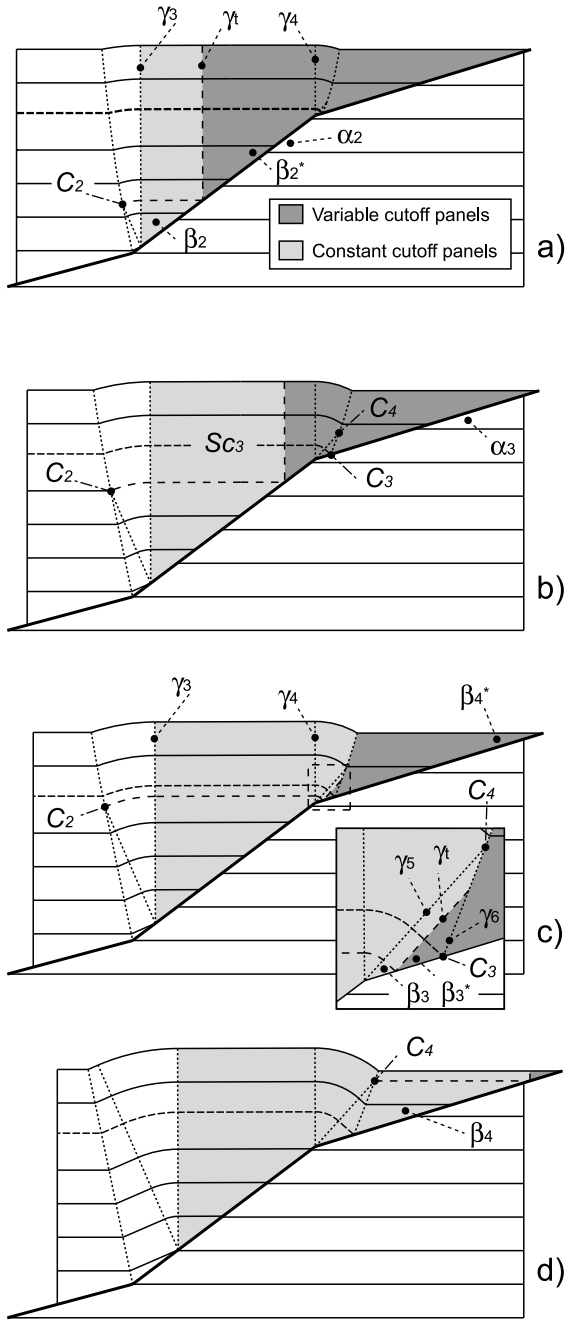

Fig. 8. Kinematic configuration of a circular fault-bend anticline in the transient stage. Upward migration of point C_2, and eventually of point C_4, produces a forelandward migration of hinge γ_t, which separates the internal sectors, characterised by constant cutoff angles, from the external sectors, characterised by variable cutoff angles.

The stratigraphical elevation of point C_2 exceeds that of point C_3 when fault displacement (S_1) verifies the following equation:

$$S_1 > Sm \bullet R \tag{87}$$

with R being the central ramp length and

$$Sm = [\sin(\beta_1)/\sin(\alpha_1)] \bullet [\sin(\phi_1) \bullet \sin(\alpha_2)]/\cos(\phi_1 - \alpha_2) \tag{86}$$

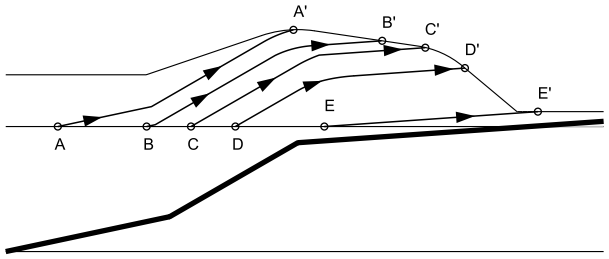

Fig. 9. Velocity field associated with the development of a curvilinear fault-bend anticline. Particle trajectories are characterised by straight segments parallel to the thrust and by parabolic segments. The latter develop above the upward convex thrust bend.

When Eq. (87) is not verified, point C_2 is still stratigraphically lower than Sc_3 (Fig. 8) and variable cutoff panels are present in the forelimb and possibly in the crestal panel.

Entering the footwall cutoff angles (α_1, α_2 and α_3) in the graphs (b) and (c) of Fig. 11 allows one to obtain a solution for the hanging wall cutoff angles. In particular, graph (b) relates α_1 and α_2 to β_1 and β_2. The central ramp hanging wall cutoff angle (β_2 or β_1, depending on fault displacement) is then entered in graph (c) to obtain the upper ramp hanging wall cutoff angle (β_3 or β_1'). When the available data are the backlimb dip (η_b), the forelimb dip (η_f), and the crestal dip in step II (η_c'), the hanging wall (α_1, α_2 and α_3) and the footwall (β_1, β_2 and β_3) cutoff angles are provided in graphs (a), (b) and (d).

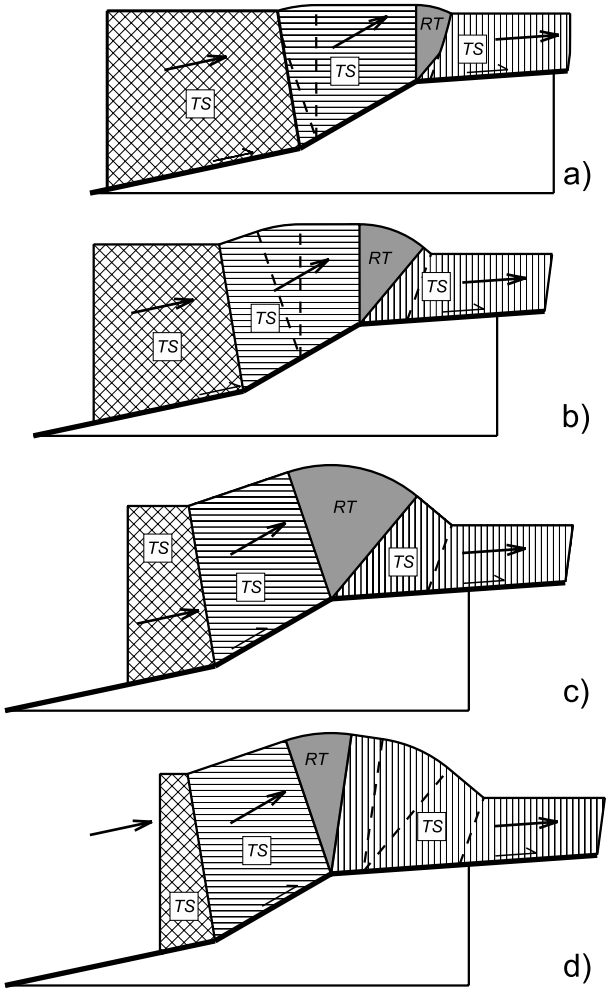

Fig. 10. Time–space evolution of translational and rototranslational sectors in a curvilinear fault-bend anticline after the transient stage.

The geometric construction of the step I configuration starts from α_2, that is obtained by linking the curvature centres of the two circular hinge sectors (Fig. 4a). The backlimb dip (η_b) and α_2 are entered into Eq. (2) to obtain β_1; α_2 and β_1 are then entered in graph (b) to obtain α_1 and β_2. Once β_2, α_2 and the forelimb dip (η_f) are known, graph (d) provides the solution for β_3. Finally, α_3 is obtained from Eq. (43). The geometric construction of the step II configuration starts from α_3, which is obtained by linking the curvature centres of the two circular hinge sectors (Fig. 4b). Entering α_3, η_f and η_c' into Eqs. (42) and (43) provides β_1' and β_3, respectively. Entering β_1', η_c' and η_b in graph (a) provides β_1. Once β_1 and η_b are known, the solution for α_2 is given by Eq. (2); α_2 and β_1 can be entered in graph (b) to obtain α_1 and β_2.

The geometrical construction of the simple step construction (Fig. 7) requires one to know either the backlimb or forelimb dip, which are univocally related (Fig. 12). For small amounts of displacement, (i.e. when γ_7 and γ_8 axial surfaces still occur), the dip of the ramp (corresponding to η_b) can be obtained by linking the curvature centre of the two circular hinge sectors.

2.6. Simplified analytical solution

The mathematical description of the internal architecture in curvilinear fault-bend anticlines can be simplified without significantly altering the overall balancing of the structures, by imposing a horizontal orientation to both the *CP* and *FL* panels. The overall error produced by these simplifications does not exceed 3% of the original line length for central ramp angles lower than 45°. At this α_2 value, the maximum difference between α_2 and β_2 is 2.3° and the maximum difference between α_3 and β_4 is 2.1°. When α_2 is 30°, the maximum difference between α_2 and β_2 is 0.2°, and the maximum difference between α_3 and β_4 is 0.2°. Moreover, the imposition of a flat lying orientation to both the *CP* and *FL* implies their constant evolution through time, eliminating the transient stage and the division between variable and constant cutoff panels. Consequently, Eq. (87) is verified for every value of slip.

3. Growth strata pattern

The occurrence of limb rotation in curvilinear fault-bend anticlines implies that rotational syngrowth wedges (e.g. Hardy and Poblet, 1994) form in the syntectonic sediments deposited on the forelimb and on the crest (Salvini et al.,

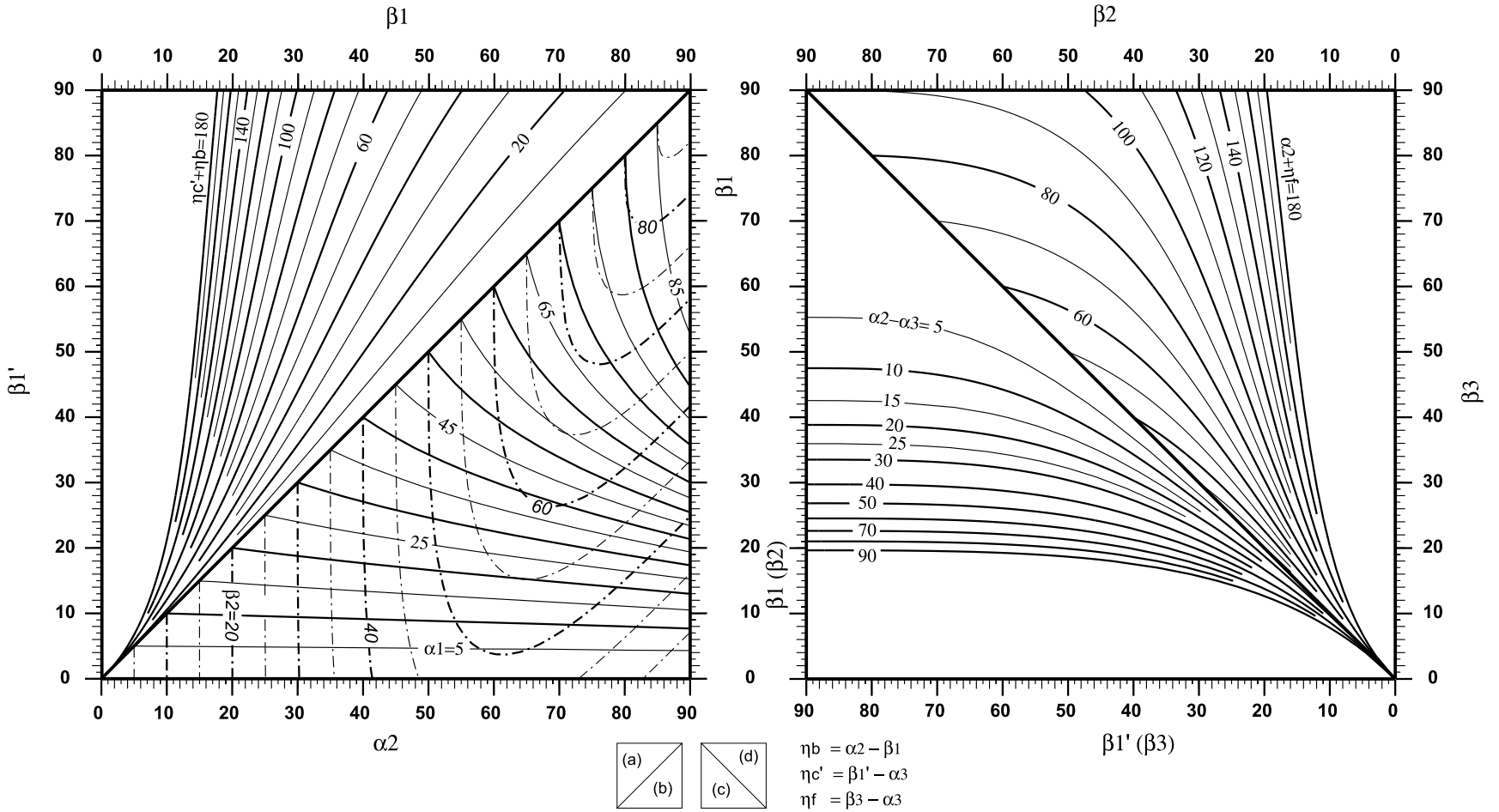

Fig. 11. Graphical solutions for the angular parameters describing curvilinear fault-bend anticlines: the graph (a) relates β_1, β_1' and the sum of η_b and η_c'. Graph (b) relates α_1, α_2, β_1 and β_2 (two parameters must be introduced in the graph). Graph (c) relates the central ramp hanging wall cutoff angle (β_1 or β_2), the upper ramp hanging wall cutoff angle (β_3 or β_1'), and the difference between α_2 and α_3. Graph (d) relates β_2, β_3 and the sum of α_2 and η_f. See text for details on the graphical construction.

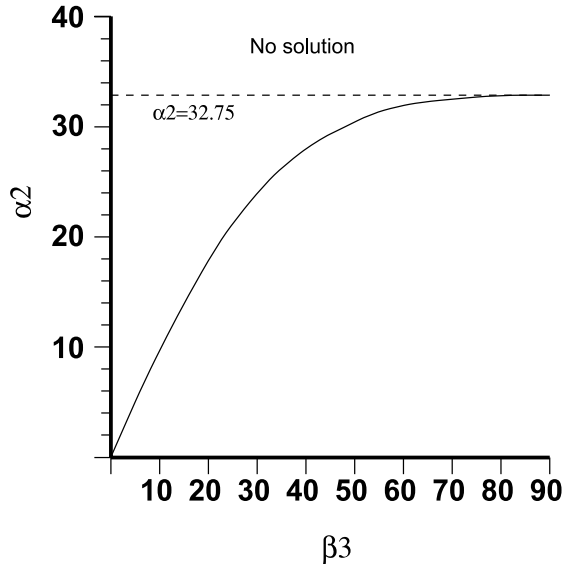

Fig. 12. Graph relating the backlimb dip ($\eta_b = \alpha_2$) to the forelimb dip (η_f) in a curvilinear fault-bend anticline when the lower and the upper ramp segments are parallel to layering (i.e. simple step, $\alpha_1 = \alpha_3 = 0$).

2001). In particular, the evolution of rototranslational sectors during fold amplification (Fig. 10) causes the development of diachronous rotational syngrowth wedges. This is clearly evident when the sedimentation rate exceeds the uplift rate of the anticlinal crest (Fig. 13). During step I, limb rotation is confined in the forelimb, and the rather steep final attitude produces well developed wedge geometries in the syntectonic sediments deposited in the leading syncline. Conversely, the nonrotational velocity field of the backlimb is highlighted by the development of a growth triangle (Suppe et al., 1992) in the syntectonic sediments deposited in the trailing syncline. Deposition of flat-lying sediments overlying the rotational syngrowth wedge in the leading syncline highlights the nonrotational velocity field of the forelimb during step II (Fig. 13d). At this stage, development of a rototranslational panel at the backlimb-crest transition produces wedge geometries in the syntectonic sediments deposited on the inner part of the crest. The lower amount of layer rotation is indicated by the smaller apical angle of the crestal rotational syngrowth wedge compared with the older rotational syngrowth wedge in the forelimb.

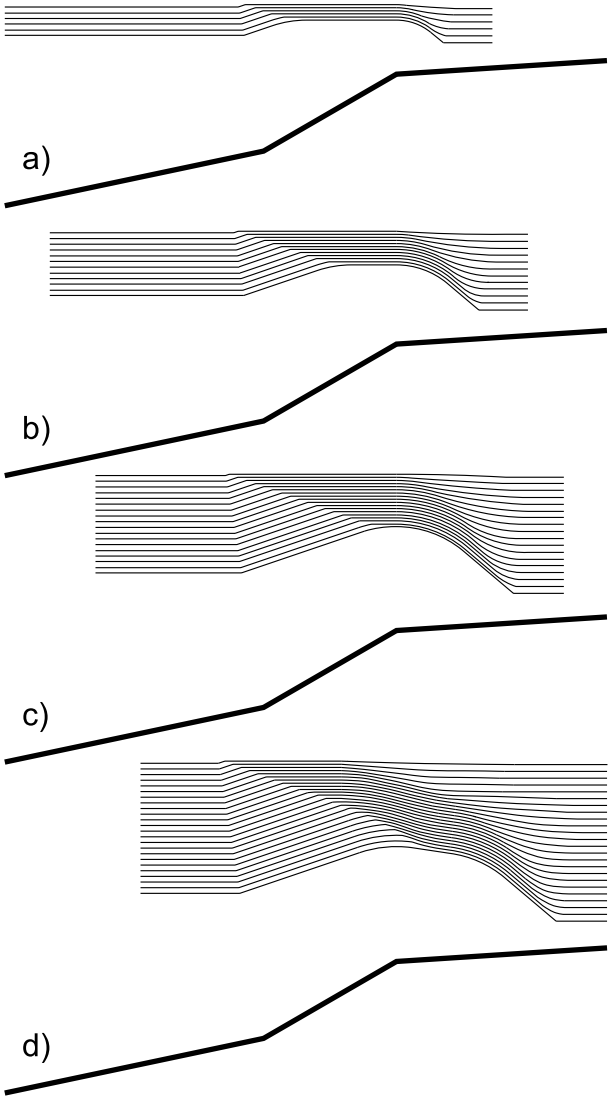

Fig. 13. Growth strata pattern predicted by curvilinear fault-bend folding. In the first stages of contraction ((a)–(c)), a growth triangle develops in the trailing syncline, while in the leading syncline a growth wedge develops. When the anticline enters in the step II configuration (d), the growth wedge developed during step I is passively transported along the upper flat and a new growth wedge develops in the crestal sector.

4. Natural examples

The Alianello anticline is located in the Sant'Arcangelo basin, Southern Apennines, Italy, and involves Pleistocene siliciclastic sediments (e.g. Pieri et al., 1994; Casciello et al., 2000). In particular, the folded multilayer consists of an alternance of conglomerates and sands. The fold axis strikes N–S and plunges about 15° toward the north. Both the backlimb-crest and crest-forelimb hinge sectors are well rounded (Fig. 14). The backlimb dip is rather constant at about 34°, and the forelimb dip is about 58°. The gentle westward dip of the foreland is related to a large-scale growth syncline (Pieri et al., 1994). Bed thickness is preserved in the pre-growth strata and shear fibres on bedding surfaces indicate flexural slip folding. Clays and conglomerates exposed in the anticlinal core are not affected by second-order folding or faulting. Growth wedges are present in the backlimb, but mainly in the forelimb. No data are available on the shape and location of the underlying blind thrust. Corresponding beds within the anticline have comparable elevations in the hinterland and at the forelimb-foreland transition, and this suggests a flat-lying décollement geometry.

Backlimb and forelimb dip data in the Alianello anticline are well fitted by curvilinear fault-bend folding (Fig. 15A

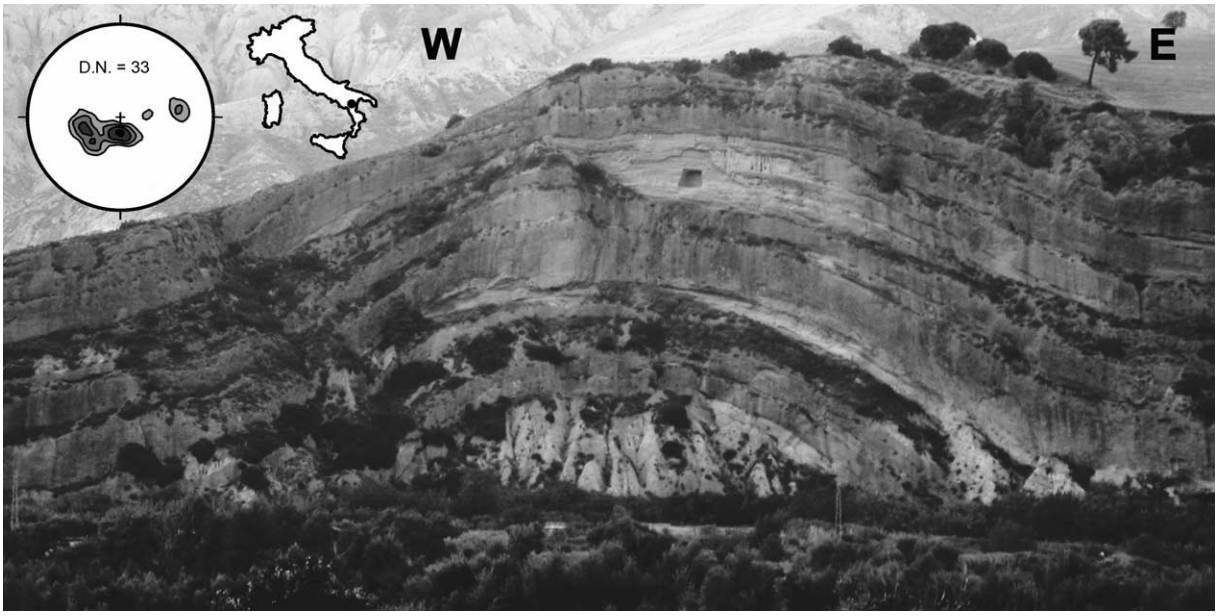

Fig. 14. Panoramic view of the Alianello anticline (Southern Apennines, Italy). The natural section is near orthogonal to the fold axis in the hinterland, in the backlimb, in the crest and in the inner part of the forelimb. Conversely, it becomes oblique in the outer part of the forelimb and in the foreland. The stereonet in the left upper corner provides the contouring of poles to bedding/lower hemisphere, 5% contouring.

and B). The model predicts an upper flat located at a very shallow depth (20 m below the ground level), and a lower flat at about 80 m below the ground level. They are connected through a 32° dipping ramp segment. The uniqueness of the geometrical solution implies that, if the Alianello anticline is interpreted as a simple step fault-bend fold, it has a Step I configuration with a fault displacement of about 90 m. Model results provide a satisfactory fit of the pre-growth strata geometry. Predicted growth stratal geometries show a rotational syngrowth wedge in the forelimb, resembling that in the Alianello anticline. Conversely, the kink-style hinge at the crest-to-backlimb transition in the model does not occur in the natural example. This mismatch can be overcome by assuming a slight segmentation of the ramp at both inflection points (Fig. 15C).

The presence of rotational syngrowth wedge in the forelimb is not predicted in kink-style fault-bend folding (Suppe et al., 1992), ruling out this model as a suitable fold kinematics for the Alianello anticline. Backlimb and forelimb dip values can be satisfactory fitted by constant thickness fault-propagation folding (Suppe and Medwedeff, 1990), assuming a 35° dipping ramp to get a 58° dipping forelimb. However, the growth strata pattern predicted by this kinematic model (Suppe et al., 1992; Storti and Poblet, 1997) consists of two growth triangles separated by a flat lying panel both in the forelimb and in the backlimb, and this does not match the geometry of syntectonic sediments in the Alianello anticline. Rotational syngrowth wedges are expected in both limbs of décollement anticlines (Poblet et al., 1997), but the lacking evidence of tectonic thickening in the Alianello core rules out this kinematic mechanism for the Alianello anticline.

The rotational syngrowth wedge geometries predicted by the curvilinear fault-bend folding are described in syntectonic sediments deposited during the evolution of natural fault-bend anticlines. In the Lost Hills anticline (Medwedeff, 1989), both the forelimb and the crestal wedges are well developed, with geometries comparable with those predicted by round-shaped fault-bend folding (Fig. 16a). The second example (Fig. 16b) shows a growth fault-bend anticline (Soto et al., 2002) associated with the Montsec thrust (Graus-Tramp basin, Southern Pyrenees), with a well-developed growth wedge in the leading syncline.

5. Discussion

5.1. Comparison with kink-style fault-bend folding

The use of circular hinge sectors to model the geometry and kinematics of fault-bend folding implies first-order differences with respect to the kink-band solution (Suppe, 1983). (1) The fold shape widens upward, both in the forelimb and in the backlimb (Fig. 3). It follows that the geometry of folded layers depends on their distance from the fault. In contrast, kink-band fault-bend folding generates constantly-dipping panels. (2) Analysing the position of circular sector curvature centres allows discrimination between Step I and Step II configurations and the unequivocal reconstruction of some aspects of the fault shape. In contrast, in kink style fault-bend folding (Fig. 5a),

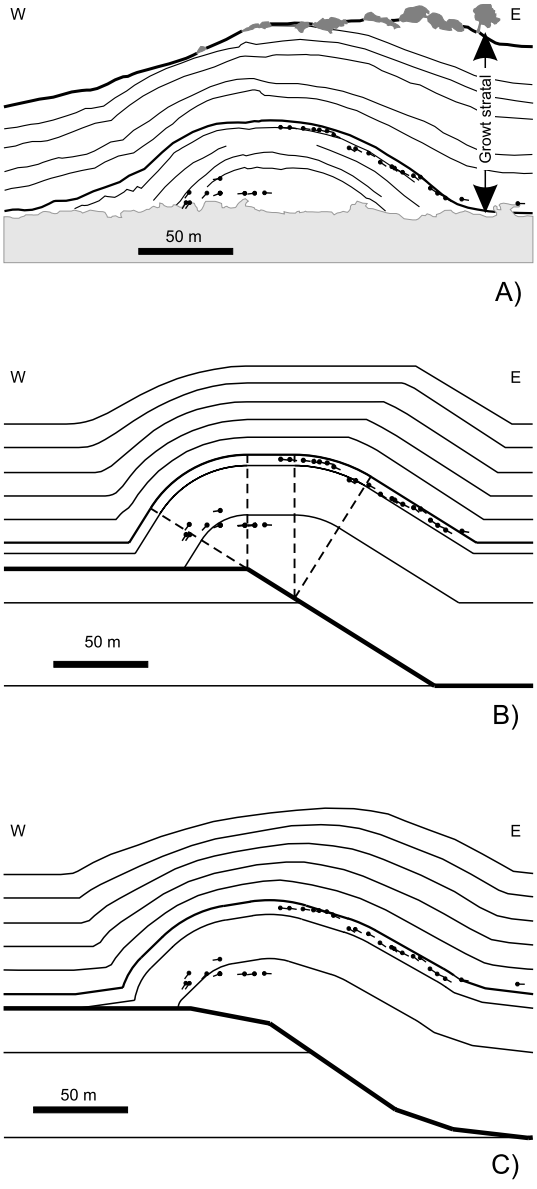

Fig. 15. Application of curvilinear fault-bend folding to the Alianello anticline. (A) Line-drawing of the photograph in Fig. 14. (B) Fold, fault and syntectonic sediments geometries resulting from the application of the curvilinear fault-bend folding with a simple step staircase fault trajectory. (C) Model results for a slightly segmented fault trajectory.

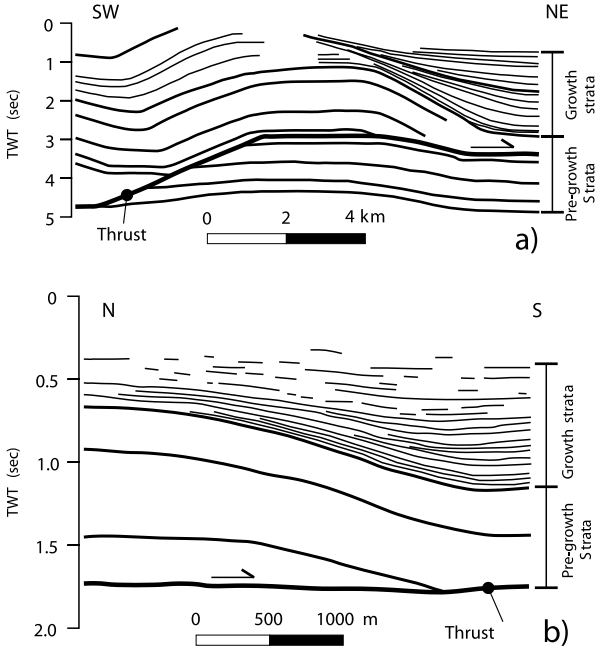

Fig. 16. Natural examples of growth stratal geometries resembling those predicted for curvilinear fault-bend anticlines. (a) Growth stratal geometries imaged in the Lost Hills anticline (after Medwedeff, 1989); (b) growth stratal geometries associated with a fault-bend anticline in the Graus–Tramp basin (after Soto et al., 2002).

fold geometry does not distinguish between large and small slip faults. (3) Curvilinear fault-bend folding predicts fault-fold angular relationships that are comparable with those obtained with the kink-band model in the most frequent range of fault ramp cutoff angles ($<30°$, e.g. Suppe, 1985). Ramp cutoff angles approaching 30° predict different forelimb dip values in the two models. In particular a steeper forelimb can be simulated by circular fault-bend folding due to steeper admissible ramp cutoff angles. In the simple step configuration, for example, the validity of the mathematical solution up to 32.75° and the asymptotic shape of the corresponding curve (Fig. 12) allow us to simulate very steep to upright forelimbs. The upper limit for the forelimb dip in a curvilinear fault-bend anticline is in fact 90°, compared with 60° in the Suppe model. (4) The presence of rototranslational sectors and consequent limb rotation in curvilinear fault-bend folding challenge the unequivocal correlation between occurrence of rotational syngrowth wedges and décollement folding as the folding mechanism (e.g. Hardy et al., 1996; Storti and Poblet, 1997). Such a correlation, which derives from the assumption of self-similar folding in fault-propagation and fault-bend anticlines (e.g. Suppe, 1985), precluded interpretation of many growth structures as fault-bend folds. (5) Conversely to the kink style model, where flexural slip is entirely accommodated within the fold, line-length balancing imposes a forelandward layer parallel shear and a hinterlandward dip in the foreland of round-shaped fault-bend anticlines. Both these geometrical outgrowths can be eliminated by assuming the occurrence of a limited amount of deformation in the foreland adjacent to the fold. In particular, depending on the environmental conditions of deformation and the mechanical stratigraphy, foreland deformation can develop by either discrete forethrusting and/or backthrusting, or/and penetrative dissolution, or/and second order folding (Fig. 17). It is worth noting, however, that the expected displacement and size of thrusting and folding induced by the predicted forelandward shear are far below the resolution of regional balanced cross-sections. Analogously, the predicted amount of layer-parallel shortening (Fig. 17d) is expected to be significantly lower than

that observed in 'undeformed' foreland, which can exceed 20% (e.g. Casas et al., 1996).

5.2. Insights for fold-related deformation

Different partitioning of bending and layer-parallel slip in the kink bands and circular hinge sectors, respectively (Fig. 2) suggests different expectations for rock fabric evolution in the various fault-bend folding models. Neglecting the role of mechanical stratigraphy, the assumption of a relationship between bending angle and deformation intensity may provide a crude approximation for predicting folding-related deformation intensity in kink-style folding (e.g. Storti and Salvini, 1996). Application of this approach to fault-bend folding (Fig. 18a) produces a deformation pattern that can be conveniently described in terms of deformation panels and deformation domains (Salvini and Storti, 2004). Deformation domains are rock volumes that contain deformational features generated by rolling of layers about active axial surfaces during a single bending event. Accordingly, this concept relates to the kinematics of the folding process. Deformation panels are rock volumes that underwent a common deformation

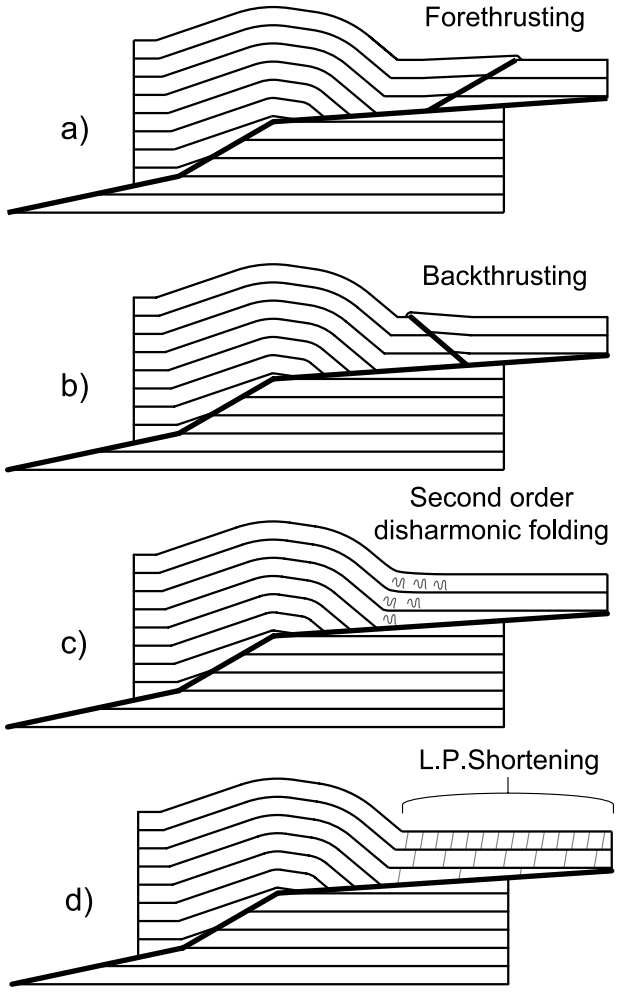

Fig. 17. Possible mechanisms suitable to annihilate the very gentle hinterlandward dip and excess layer-parallel slip in the foreland of curvilinear fault-bend anticlines: (a) second-order forethrusting; (b) second-order backthrusting; (c) second order disharmonic folding; (d) stratabound pressure solution with an upward increasing intensity.

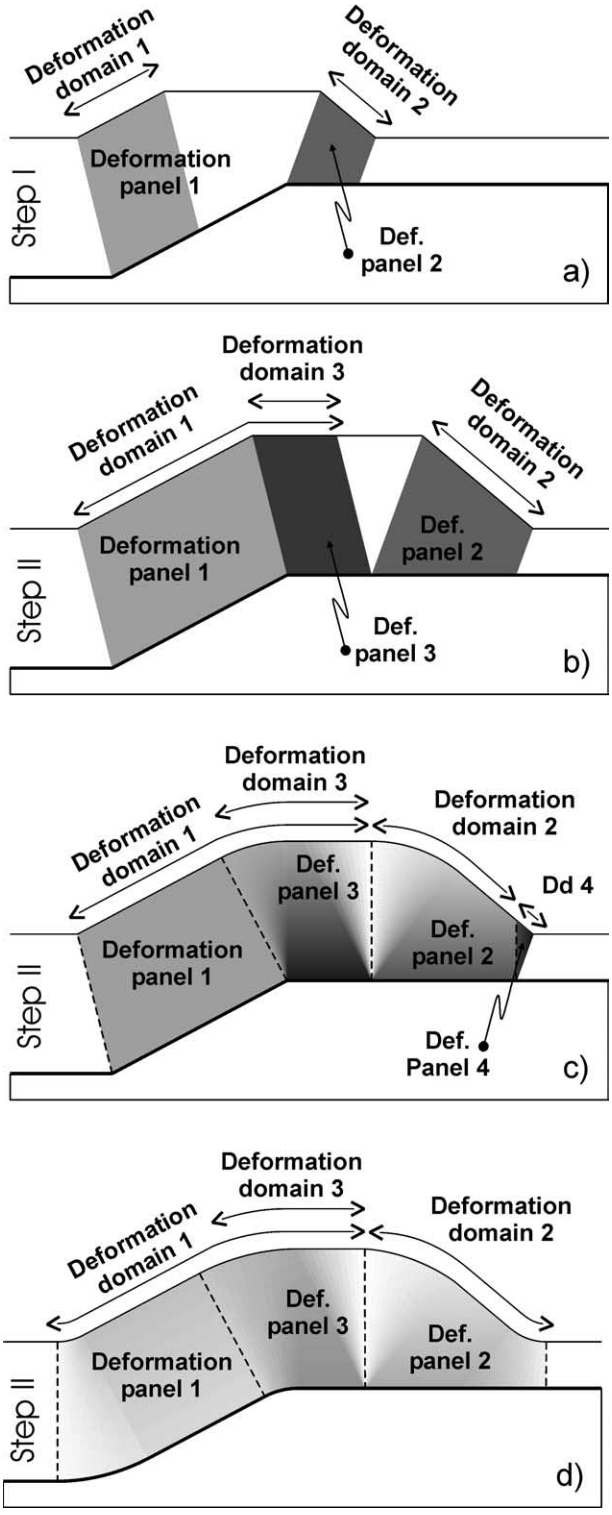

Fig. 18. Distribution of deformation panels and deformation domains in kink-style fault-bend folding ((a) and (b)) and curvilinear fault-bend folding ((c) and (d)). Grey tones are proportional to the expected deformation intensity. See text for details.

history. This concept relates to the deformation fabric of a given rock volume. Deformation panels and deformation domains coincide in step I fault-bend folding (Fig. 18a). During step II, the inner crestal panel belongs to both the deformation domains 1 and 3, and corresponds to deformation panel 3, produced by the overprinting of two bending events (Salvini and Storti, 2004) (Fig. 18b). Application of these concepts to kink-style fault-bend folding in material with homogeneous mechanical stratigraphy, systematically produces uniformly deformed rock panels (e.g. Salvini and Storti, 2001).

Material passing through a circular hinge undergoes a bedding-plane slip whose cumulative value is constant, while its increment per time is dependent on the distance from the curvature centre, as well as the curvature itself. This may imply a more smoothed and non-homogeneous distribution of deformational features in the folded rock panels. Development of curvilinear fault-bend anticlines above staircase thrust trajectories produces deformation panels associated with both kink-style and circular hinges (Fig. 18c). In particular, material migration about the lower ramp inflection point causes homogeneous deformation in rock folded by the straight hinge segment γ_1, whereas rocks rolling about the parabolic hinge γ_7 undergo a non-homogeneous deformation, roughly proportional to layer dip. This implies that the backlimb of the fault-bend anticline during step I (Fig. 7) is expected to consist of a non-homogeneously deformed rock panel (BP') ahead of a homogeneously deformed one (BP). The completion of the structure during step II eventually results in a deformation pattern consisting of four deformation panels (Fig. 18c). The innermost one, in the backlimb, is predicted to be homogeneously deformed, analogous to the kink-style structure. Deformation in the other three panels is non-uniformly distributed and its intensity generally decreases upward and laterally. Comparison with a kink-style fault-bend anticline highlights similar patterns of deformation domains/panels in the backlimb and crest, significant intensity differences in the deformation panels 2 and an important size reduction of the crestal region virtually unaffected by folding related deformation. Deformation panel/domain 4 characterises the frontal sector of the forelimb in curvilinear fault-bend anticlines and develop by instantaneous bending of foreland material about axial surface γ_8, followed by progressive forelandward rotation.

Adoption of more smoothed geometries at both the lower and upper ramp inflection points, increases the width of hinge zones (Fig. 18d). In particular, kink-style hinges at the lower ramp inflection point and at the forelimb–foreland transition are replaced by curvilinear hinge sectors. Progressive layer curvature by parallel folding at the hinterland–backlimb transition, induces an upward increasing gradient in deformation intensity, opposite to folding at the upper ramp inflection zone. As a consequence, the average intensity of deformation in panel 3 decreases compared with that expected in curvilinear fault-bend anticlines developed above staircase thrust trajectories. The general decrease of deformation intensity all along the anticline is not homogeneous and this attenuates differences among deformation panels (Fig. 18d). Finally, the widening of the forelimb–foreland transition implies the narrowing of the deformation panel 4 and eventually its annihilation. Comparison between predicted deformation patterns in kink-style fault-bend folding and curvilinear fault-bend folding shows that in the latter deformation intensity is not a diagnostic parameter for identifying deformation domains/panels. Dip and typology (i.e. fault, joint, solution cleavage) of deformational features and their possible overprinting relationships (e.g. Srivastava and Engelder, 1990) may provide a valuable tool for such a purpose in curvilinear fault-bend anticlines. Identifying deformation domains/panels provides, in fact, an effective support for correctly unravelling fold-fault kinematics (e.g. Salvini and Storti, 2004).

6. Conclusions

Circular hinge sectors have been used to analytically model the geometry and kinematics of fault-bend folding (curvilinear fault-bend folding). The analytical solution of curvilinear fault-bend folding predicts fault-fold angular relationships that are comparable with that provided by the classical kink-style model in the commonly accepted range of fault ramp cutoff angles ($<30°$). However, the geometry of the fold and, above all, its kinematic evolution, are different. In particular, the velocity field of round-shaped fault-bend folding consists of translational (non-rotational) and rototranslational sectors where the distance of particles from the fault varies through time. The presence of rototranslational sectors implies the occurrence of limb rotation in the forelimb and in the crest that, when sedimentation occurs contemporary to folding, produces rotational syngrowth wedges in the syntectonic sediments. Limb rotation occurs diachronously during the evolution of a curvilinear fault-bend anticline and, consequently, the syngrowth wedge in the forelimb predates the one in the crest.

Circular hinge sectors allow one to successfully model rounded fold shapes without implying a great segmentation of the fault shape. This, coupled with the predicted development of rotational syngrowth wedges, broadens the applicability of fault-bend folding for modelling the evolution and internal architecture of natural thrust related anticlines. Line-length balancing imposes the occurrence of a hinterlandward dipping panel and of an excess forelandward layer-parallel shear in the foreland of curvilinear fault-bend anticlines. This ‘excess length’ in the foreland may provide the proper triggering factor for second-order folding and faulting, and pressure solution cleavages that are commonly found at the toe of shallow foreland structures. Application of model predictions to natural thrust-related

anticlines validates the usefulness of the proposed geometrical and analytical solution.

Acknowledgements

We gratefully acknowledge constructive criticism and advice from D.A. Medwedeff, N. Woodward and an anonymous reviewer, which helped us to significantly improve an early version of the manuscript.

Appendix A

A.1. Equations 1 and 2 (see Fig. 19b)

$$\phi_1 = (\alpha_2 - \beta_1)/2 \quad (1)$$

$$\eta_b = \alpha_2 - \beta_1 \quad (2)$$

A.2. Equation 9 (see Fig. 19a and b)

After migration across the axial surface $\gamma 1$, the triangle ABL (Fig. 19a) becomes A′BL (Fig. 19b). In order to preserve line length, AB must equal A′B:

$$AB = \sin(90 + \phi_1 - \alpha_1)\bullet[AL/\sin(\alpha_1)] \quad (3)$$

$$A'B = \sin(90 + \phi_1 - \alpha_2)\bullet[AL/\sin(\beta_1)] \quad (4)$$

By comparing Eqs. (3) and (4) we obtain:

$$\cos(\phi_1 - \alpha_2)/\sin(\beta_1) = \cos(\phi_1 - \alpha_1)/\sin(\alpha_1) \quad (5)$$

$\cos(\phi_1 - \alpha_2)$ can also be expressed as $\cos(\phi_1 + \beta_1)$, and Eq. (5) becomes:

$$\cos(\phi_1 + \beta_1)/\sin(\beta_1) = [\cos(\phi_1)\bullet\cos(\alpha_1) + \sin(\phi_1)\bullet\sin(\alpha_1)]/\sin(\alpha_1) \quad (6)$$

Eq. (6) can also be written as:

$$[\cos(\phi_1)\bullet\cos(\beta_1) - \sin(\phi_1)\bullet\sin(\beta_1)]/\sin(\beta_1) = \cos(\phi_1)\bullet\cot(\alpha_1) + \sin(\phi_1) \quad (7)$$

Simplifying and rearranging:

$$\cot(\alpha_1) = \cot(\beta_1) - 2\tan(\phi_2) \quad (8)$$

Substituting Eq. (1) into Eq. (8):

$$\cot(\alpha_1) = \cot(\beta_1) - 2\tan[(\alpha_2 - \beta_1)/2] \quad (9)$$

A.3. Equations 17–19 (see Fig. 19a and b)

During shortening, the shape of polygon ABCDEFG (Fig. 19a) modifies to A′BCDEF′G′H (Fig. 19b). Line length preservation imposes:

$$EF + FG = EF' + F'G' + G'H \quad (10)$$

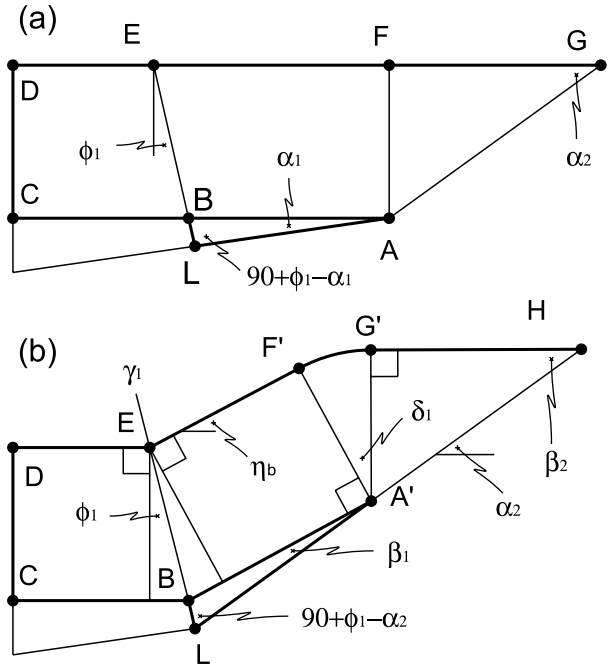

Fig. 19. Geometrical construction for Eqs. (1), (2), (9), (17)–(19) and (48).

$$EF = AB + CD\bullet\tan(\phi_1) \quad (11)$$

$$FG = CD\bullet\cot(\alpha_2) \quad (12)$$

$$EF' = AB - CD\bullet\tan(\phi_1) \quad (13)$$

$$F'G' = CD\bullet\delta_1 \quad (14)$$

$$G'H = CD\bullet\cot(\beta_2) \quad (15)$$

Substituting Eqs. (11)–(15) into Eq. (10) and simplifying:

$$\delta_1 + \cot(\beta_2) - 2\tan(\phi_1) = \cot(\alpha_2) \quad (16)$$

$$\delta_1 = \beta_2 - \beta_1 \quad (17)$$

Substituting Eqs. (17) and (1) into Eq. (16) we obtain:

$$\cot(\beta_2) + \beta_2 = \cot(\alpha_2) - \cot(\alpha_1) + \cot(\beta_1) + \beta_1 \quad (18)$$

$$\eta_c = \alpha_2 - \beta_2 \quad (19)$$

A.4. Equations 25a, 25b, 26a and 26b (see Fig. 20a and b)

After translation onto the upper ramp, triangle ABC becomes the polygon ABC′D (Fig. 20). Line length preservation requires that:

$$BC = BC' + C'D \quad (20)$$

$$BC = AB\bullet\cot(\beta_2 \text{ or } \beta_1) \quad (21)$$

being either β_2 (Step I) or β_1 (Step II) the hanging wall central ramp cut-off angles:

$$BC' = AB \bullet (\delta_2 \text{ or } \delta_1') \quad (22)$$

where either δ_2 (Step I) or δ_1' (Step II) are the apical angles of the circular sector pinned at the central ramp upper inflection point:

$$C'D = AB \bullet \cot(\beta_3 \text{ or } \beta_1') \quad (23)$$

being β_3 (Step I) or β_1' (Step II) the forelimb or the CP' panel cutoff angle.

Substituting Eqs. (21)–(23) into Eq. (20) and simplifying:

$$\cot(\beta_2 \text{ or } \beta_1) = (\delta_2 \text{ or } \delta_1') + \cot(\beta_3 \text{ or } \beta_1') \quad (24)$$

$$\delta_2 = \beta_3 - \beta_2 + \alpha_2 - \alpha_3 \quad (25a)$$

$$\delta_1' = \beta_1' - \beta_1 + \alpha_2 - \alpha_3 \quad (25b)$$

Substituting Eqs. (25a) or (25b) into Eq. (24) we obtain:

$$\cot(\beta_3) + \beta_3 = \alpha_3 - \alpha_2 + \cot(\beta_2) + \beta_2 \quad (26a)$$

$$\cot(\beta_1') + \beta_1' = \alpha_3 - \alpha_2 + \cot(\beta_1) + \beta_1 \quad (26b)$$

A.5. Equation 28 (see Fig. 21b)

$$\phi_2 = 90 - [180 - (\beta_3 - \alpha_3) - (\alpha_3 - \beta_4)]/2 \quad (27)$$

Simplifying:

$$\phi_2 = (\beta_3 - \beta_4)/2 \quad (28)$$

A.6. Equation 41 (see Fig. 21a and b)

During contraction, triangle ACD (Fig. 21a) becomes AC′D′ (Fig. 21b). Line length preservation imposes:

$$CD = C'D - AC' \quad (29)$$

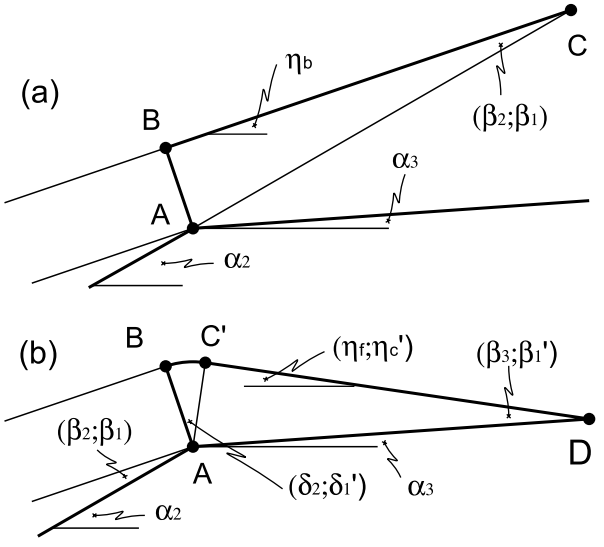

Fig. 20. Geometrical construction for Eqs. (25a), (25b), (26a), (26b), (42), (43), (52a) and (52b).

$$CD = H \bullet \cot(\alpha_3) - H \bullet \cot(\alpha_2) \quad (30)$$

$$B'C' = H/\cos(\phi_2) \quad (31)$$

$$C'D' = B'C' \bullet [\sin(90 + \phi_2 - \beta_3)/\sin(\beta_4)] \quad (32)$$

$$AC' = B'C' \bullet [\sin(90 + \phi_2 - \beta_3)/\sin(\beta_3)] \quad (33)$$

Substituting Eq. (31) into Eqs. (32) and (33), we obtain:

$$C'D' = H \bullet [\cos(\phi_2 - \beta_3)/\sin(\beta_4)]/\cos(\phi_2) \quad (34)$$

$$AC' = H \bullet [\cos(\phi_2 - \beta_3)/\sin(\beta_3)]/\cos(\phi_2) \quad (35)$$

Substituting Eqs. (30), (34) and (35) into Eq. (29) and simplifying:

$$[\cos(\phi_2 - \beta_3)/\cos(\phi_2)] \bullet [1/\sin(\beta_4) - 1/\sin(\beta_3)] = \cot(\alpha_3) - \cot(\alpha_2) \quad (36)$$

Eq. (36) can also be written as:

$$\cos(\phi_2 - \beta_3)/[\cos(\phi_2) \bullet \sin(\beta_4)] - \cos(\phi_2 - \beta_3)/[\cos(\phi_2) \bullet \sin(\beta_3)] = \cot(\alpha_3) - \cot(\alpha_2) \quad (37)$$

$\cos(\phi_2 - \beta_3)$ can also be written as $\cos(\phi_2 + \beta_4)$, which substituted into Eq. (37) gives:

$$\cos(\phi_2 + \beta_4)/[\cos(\phi_2) \bullet \sin(\beta_4)] - \cos(\phi_2 - \beta_3)/[\cos(\phi_2) \bullet \sin(\beta_3)] = \cot(\alpha_3) - \cot(\alpha_2) \quad (38)$$

Eq. (38) can be written as:

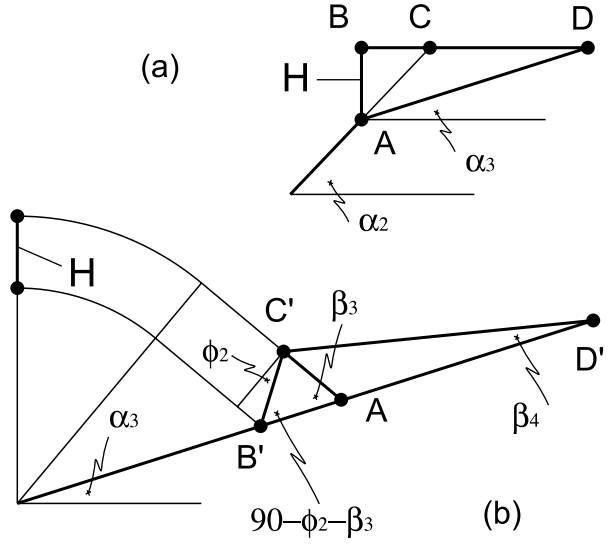

Fig. 21. Geometrical construction for Eqs. (28) and (41).

$$\{[\cos(\phi_2)\bullet\cos(\beta_4) - \sin(\phi_2)\bullet\sin(\beta_4)]/[\cos(\phi_2)\bullet\sin(\beta_4)]\} - \{[\cos(\phi_2)\bullet\cos(\beta_3) + \sin(\phi_2)\bullet\sin(\beta_3)]/[\cos(\phi_2)\bullet\sin(\beta_3)]\} = \cot(\alpha_3) - \cot(\alpha_2) \quad (39)$$

Simplifying and rearranging:

$$\cot(\beta_4) - \cot(\beta_3) - 2\tan(\phi_2) = \cot(\alpha_3) - \cot(\alpha_2) \quad (40)$$

Substituting Eq. (28) into Eq. (40):

$$\cot(\beta_4) - 2\tan[(\beta_3 - \beta_4)/2] = \cot(\alpha_3) - \cot(\alpha_2) + \cot(\beta_3) \quad (41)$$

A.7. Equations 42 and 43 (see Fig. 20a and b)

$$\eta'_c = \beta'_1 - \alpha_3 \quad (42)$$

$$\eta_f = \beta_3 - \alpha_3 \quad (43)$$

A.8. Equation 45 (see Fig. 4)

$$\delta'_1 + \delta'_2 = \delta_1 + \delta_2 \quad (44)$$

Substituting Eqs. (18), (25a) and (25b) into Eq. (44) and simplifying:

$$\delta'_2 = \beta_3 - \beta'_1 \quad (45)$$

A.9. Equations 48, 52a and 52b (see Figs. 19 and 20)

The relationships between the total shortening along the lower ramp (S_1) and its partitioning in the central (S_2) and upper (S_3) ramps are described by Eqs. (48), (52a) and (52b). In particular, when the amount of slip along the lower ramp (S_1) is LA (Fig. 19), the amount of slip along the central ramp (S_2) is LA′ and the following equations are verified:

$$\mathrm{LB} = S_1\bullet\sin(\alpha_1)/\cos(\phi_1) \quad (46)$$

$$S_2/\sin[180 - (90 + \phi_1 - \alpha_2) - \beta_1] = \mathrm{LB}/\sin(\beta_1) \quad (47)$$

Substituting Eq. (46) into Eq. (47) and simplifying we obtain:

$$S_2 = S_1\bullet\sin(\alpha_1)/\sin(\beta_1) \quad (48)$$

which relates the amount of shortening along the lower and central ramps.

When the incremental shortening along the central ramp (S_2) equals AC (Fig. 20), the amount of slip along the upper ramp (S_3) is AD:

$$\mathrm{AB} = S_2/\sin(\beta_2;\ \beta_1) \quad (49)$$

$$S_3 = \mathrm{AB}/\sin(\beta_3;\ \beta'_1) \quad (50)$$

Substituting Eq. (49) into Eq. (50) and simplifying:

$$S_3 = S_2\bullet[\sin(\beta_2;\ \beta_1)/\sin(\beta_3;\ \beta'_1)] \quad (51)$$

Substituting Eq. (48) into Eq. (51), we obtain:

$$S_3 = S_1\bullet[\sin(\alpha_1)/\sin(\beta_1)]\bullet[\sin(\beta_2)/\sin(\beta_3)] \quad (52a)$$

which relates the amount of shortening along the lower and upper ramp in the step I configuration.

During step II, the hanging wall cut-off angles along the central and upper ramp become β_1 and β'_1, respectively. As a consequence, Eq. (52a) becomes:

$$S'_3 = S'_1\bullet[\sin(\alpha_1)/\sin(\beta_1)]\bullet[\sin(\beta_1)/\sin(\beta'_1)] \quad (52b)$$

with S'_3 and S'_1 being the amount of slip after the transition from step I to step II.

A.10. Equations 53, 54 and 56 (see Fig. 22a)

These describe the incremental position of C_2 during the fold evolution, calculated with respect to C_1 (0,0):

$$Y_{C2} = D_{C2}\bullet\cos(\alpha_2 - \beta_1) \quad (53)$$

$$X_{C2} = -D_{C2}\bullet\sin(\alpha_2 - \beta_1) \quad (54)$$

with X_{C2} and Y_{C2} being the incremental coordinates of C_2 at shortening S_1:

$$S_2/\sin(\phi_1) = D_{C2}/\sin(90 - \alpha_2 + \phi_1) \quad (55)$$

Substituting Eq. (48) into Eq. (55) and rearranging:

$$D_{C2} = S_1\bullet[\sin(\alpha_1)/\sin(\beta_1)]\bullet[\cos(\alpha_2 - \phi_1)/\sin(\phi_1)] \quad (56)$$

A.11. Equations 58, 59 and 63 (see Fig. 22b)

These describe the incremental position of C_4, respect to the upper inflection point of the central ramp I_2 (0,0):

$$D_{C4} = \mathrm{L1} + \mathrm{L2} \quad (57)$$

$$Y_{C4} = D_{C4}\bullet\cos(\delta_2) \quad (58)$$

$$X_{C4} = D_{C4}\bullet\sin(\delta_2) \quad (59)$$

with X_{C4} and Y_{C4} being the incremental coordinates of C_4 at shortening S_1:

$$\mathrm{L1} = S_3\bullet\sin(\beta_3) \quad (60)$$

$$\mathrm{L2} = S_3\bullet\cos(\beta_3)/\tan(\phi_2) \quad (61)$$

Substituting Eqs. (62) and (63) into Eq. (57):

$$D_{C4} = S_3\bullet[\sin(\beta_3) + \cos(\beta_3)/\tan(\phi_2)] \quad (62)$$

Substituting Eq. (52a) into Eq. (62) and simplifying:

$$D_{C4} = S_1\bullet[\sin(\alpha_1)/\sin(\beta_1)]\bullet[\sin(\beta_2)]\bullet[1 + \cot(\beta_3)\bullet\cot(\phi_2)] \quad (63)$$

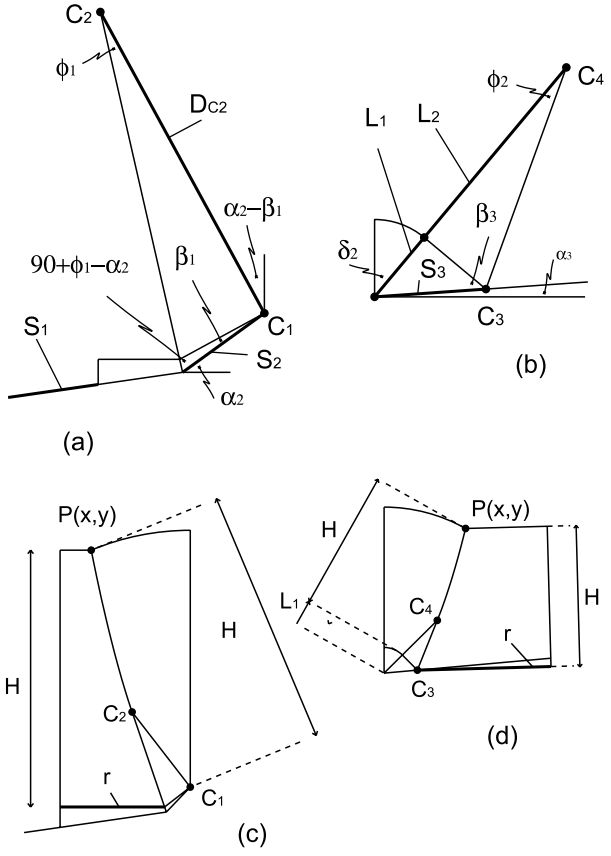

Fig. 22. Geometrical construction for Eqs. (86), (87), (53), (54), (56), (58), (59), (63), (66), (68), (81) and (83).

A.12. Equations 66 and 68 (see Fig. 22c)

These describe the parabolic shape of γ_7, which is the locus of the points whose distance from C_1 and from the line r is constant, with C_1 being the origin of the reference Cartesian system:

$$r: y = -S_2 \bullet \sin(\alpha_2) + S_1 \bullet \sin(\alpha_1) \tag{64}$$

Substituting Eq. (48) into Eq. (64) and rearranging:

$$r: y = S_1 \bullet [\sin(\alpha_1)/\sin(\beta_1)] \bullet [\sin(\beta_1) - \sin(\alpha_2)] \tag{65}$$

$$K = S_1 \bullet [\sin(\alpha_1)/\sin(\beta_1)] \bullet [\sin(\alpha_2) - \sin(\beta_1)] \tag{66}$$

Substituting Eq. (66) into Eq. (65):

$$r: y = -K \tag{67}$$

The solution for γ_7 is:

$$y = x^2/2K - K/2 \tag{68}$$

A.13. Equations 81 and 83 (see Fig. 22d)

These describe the parabolic shape of γ_8, which is the locus of the points whose distance from the central ramp upper inflection point is H+L1 and whose distance from the line r is H:

$$\mathrm{L1} = S_3 \bullet \sin(\beta_3) \tag{69}$$

$$r: y = x \bullet \tan(\alpha_3 - \beta_4) + S_3 \bullet [\sin(\alpha_3) - \cos(\alpha_3) \bullet \tan(\alpha_3 - \beta_4)] \tag{70}$$

$$J = [\sin(\alpha_3) - \cos(\alpha_3) \bullet \tan(\alpha_3 - \beta_4)] \tag{71}$$

The distance between point P and the line r is equal to H and it is given by the following equation:

$$\mathrm{H} = -[x \bullet \tan(\alpha_3 - \beta_4) - y + J]/[\tan^2(\alpha_3 - \beta_4) + 1]^{1/2} \tag{72}$$

Simplifying:

$$\mathrm{H} = [-x \bullet \tan(\alpha_3 - \beta_4) + y - J] \bullet \cos(\alpha_3 - \beta_4) \tag{73}$$

The distance between P and the origin (I_2) is D1, which is also equal to H+L1. The distance between P and r is H. It follows that:

$$\mathrm{D1} - \mathrm{L1} = \mathrm{H} \tag{74}$$

$$\mathrm{D1}^2 = (\mathrm{H} + \mathrm{L1})^2 \tag{75}$$

$$\mathrm{D1}^2 = x^2 + y^2 \tag{76}$$

Substituting Eqs. (69), (73) and (76) into Eq. (75) and rearranging:

$$x^2 + y^2 = \{[-x \bullet \tan(\alpha_3 - \beta_4) + y - S_3 * J] \bullet \cos(\alpha_3 - \beta_4) + [S_3 \bullet \sin(\beta_3)]\}^2 \tag{77}$$

Simplifying:

$$x^2 + y^2 = \{[-x \bullet \sin(\alpha_3 - \beta_4) + y \bullet \cos(\alpha_3 - \beta_4) - S_3 \bullet J \bullet \cos(\alpha_3 - \beta_4)] + [S_3 \bullet \sin(\beta_3)]\}^2 \tag{78}$$

$$\begin{aligned} &J \bullet \cos(\alpha_3 - \beta_4) = [\sin(\alpha_3) - \cos(\alpha_3) \bullet \tan(\alpha_3 - \beta_4)] \bullet \cos(\alpha_3 - \beta_4) \\ &= \sin(\alpha_3) \bullet \cos(\alpha_3 - \beta_4) - \cos(\alpha_3) \bullet \sin(\alpha_3 - \beta_4) \\ &= \sin[\alpha_3 - (\alpha_3 - \beta_4)] = \sin(\beta_4) \end{aligned} \tag{79}$$

Substituting Eq. (79) into Eq. (78) and reassembling:

$$x^2 + y^2 = \{-x \bullet \sin(\alpha_3 - \beta_4) + y \bullet \cos(\alpha_3 - \beta_4) - S_3 \bullet [\sin(\beta_4) - \sin(\beta_3)]\}^2 \tag{80}$$

$$K = S_3 \bullet [\sin(\beta_3) - \sin(\beta_4)] \tag{81}$$

Substituting Eq. (81) into Eq. (80) and rearranging:

$$x^2 + y^2 = [x \bullet \sin(\alpha_3 - \beta_4)]^2 + [y \bullet \cos(\alpha_3 - \beta_4)]^2 + K^2 - 2xy \bullet [\sin(\alpha_3 - \beta_4) \bullet \cos(\alpha_3 - \beta_4)] - 2Kx \bullet \sin(\alpha_3 - \beta_4) + 2Ky \bullet \cos(\alpha_3 - \beta_4) \quad (82)$$

Simplifying and reassembling we obtain:

$$[X \bullet \cos(\alpha_3 - \beta_4) + Y \bullet \sin(\alpha_3 - \beta_4)]^2 = K \bullet [-2x \bullet \sin(\alpha_3 - \beta_4) + 2y \bullet \cos(\alpha_3 - \beta_4) + K] \quad (83)$$

This equation describes the shape of γ_8 being the central ramp upper inflection point I_2 (0,0), the origin of the reference Cartesian system.

A.14. Equations 86 and 87 (see Figs. 4 and 22a)

D_{C2} must exceed the thickness of the 'stratigraphical distance' between the upper (I_2) and lower (I_1) central ramp inflection points:

$$D_{C2} > (R) \bullet \sin(\alpha_2) \quad (84)$$

with R being the central ramp length.

Substituting Eq. (56) into Eq. (84) and rearranging:

$$S_1 > R \bullet [\sin(\alpha_2) \bullet \sin(\beta_1) \bullet \sin(\phi_1)]/[\sin(\alpha_1) \bullet \cos(\alpha_2 - \phi_1)] \quad (85)$$

$$Sm = [\sin(\beta_1)/\sin(\alpha_1)] \bullet [\sin(\phi_1) \bullet \sin(\alpha_2)]/\cos(\phi_1 - \alpha_2) \quad (86)$$

Substitution of Eq. (86) into Eq. (85):

$$S_1 > Sm \bullet R \quad (87)$$

References

Busk, H.G., 1929. Earth Flexures. Cambridge University Press, Cambridge. 106pp.

Casas, J.M., Durney, D., Ferret, J., Munoz, J.A., 1996. Determinacion de la deformacion finita en la vertiente sur del Pirineo oriental a lo largo de la transversal del rio Ter. Geogaceta 20, 803–805.

Casciello, E., Cesarano, M., Ferranti, L., Oldow, J.S., Pappone, G., 2000. Pleistocene non-coaxial fold development in the northern portion of the S. Arcangelo basin (Southern Apennines). Memorie Società Geologica Italiana 55, 133–140.

Chester, J.S., 2003. Mechanical stratigraphy and fault–fold interaction, Absaroka thrust sheet, Salt River Range, Wyoming. Journal of Structural Geology 25, 1171–1192.

Chester, J.S., Chester, F.M., 1990. Fault-propagation folds above thrusts with constant dip. Journal of Structural Geology 12, 903–910.

Corbett, K., Friedmean, M., Spang, J., 1987. Fracture development and mechanical stratigraphy of Austin Chalk, Texas. American Association of Petroleum Geologists Bulletin 71, 17–28.

Dahlstrom, C.D.A., 1969. The upper detachment in concentric folding. Canadian Society of Petroleum Geology Bulletin 18, 332–406.

Dahlstrom, C.D.A., 1990. Geometric constraints derived from the law of conservation of volume and applied to evolutionary models for detachment folding. American Association of Petroleum Geologists Bulletin 74, 336–344.

De Sitter, L.V., 1956. Structural Geology. McGraw Hill, New York.

Elliott, D., 1983. The construction of balanced cross-sections. Journal of Structural Geology 5, 101.

Epard, J.-L., Groshong Jr., R.H., 1995. Kinematic model of detachment folding including limb rotation, fixed hinges and layer-parallel strain. Tectonophysics 247, 85–103.

Faill, R.T., 1969. Kink band structure in the Valley and Ridge province, central Pennsylvania. Geological Society of America Bulletin 80, 2539–2550.

Faill, R.T., 1973. Kink band folding: Valley and Ridge province, Pennsylvania. Geological Society of America Bulletin 84, 1289–1314.

Fischer, M.B., Jackson, P.B., 1999. Stratigraphic controls on deformation patterns in fault-related folds: a detachment fold example from the Sierra Madre Oriental, northeast Mexico. Journal of Structural Geology 21, 613–633.

Fowler, T.J., Winsor, C.N., 1997. Characteristics and occurrence of bedding-parallel slip surfaces and laminated veins in chevron folds from the Bendingo–Castelmaine goldfields: implications for flexural-slip folding. Journal of Structural Geology 19, 799–815.

Hardy, S., 1995. A method for quantifying the kinematics of fault-bend folding. Journal of Structural Geology 17, 1785–1788.

Hardy, S., Poblet, J., 1994. Geometric and numerical model of progressive limb rotation in detachment folds. Geology 22, 371–374.

Hardy, S., Poblet, J., McClay, K., Waltham, D., 1996. Mathematical modelling of growth strata associated with fault-related fold structures. Special Publication of the Geological Society 99, 265–282.

Homza, T.X., Wallace, W.K., 1995. Geometric and kinematic model for detachment fold with fixed and variable detachment depth. Journal of Structural Geology 17, 575–588.

Jamison, W.R., 1992. Stress controls of fold thrust style, in: McClay, K.R. (Ed.), Thrust Tectonics. Chapman and Hall, London, pp. 155–164.

Jamison, W.R., 1997. Quantitative evaluation of fractures on Monkshood anticline, a detachment fold in the Foothills of Western Canada. The American Association of Petroleum Geologist Bulletin 81, 1110–1132.

Jamison, W.R., Pope, A., 1996. Geometry and evolution of a fault-bend fold: Mount Bertha anticline. Geological Society of America Bulletin 108, 208–224.

Julivert, M., Arboleya, M., 1984. A geometrical and kinematical approach to the nappe structure in an arcuate fold belt: the Cantabrian nappes (Hercynian chain, NW Spain). Journal of Structural Geology 6, 449–519.

Medwedeff, D., 1989. Growth fault-bend folding at southeast Lost Hills, San Joaquin Valley, California. American Association Petroleum Geology Bulletin 73, 54–67.

Medwedeff, D.A., Suppe, J., 1997. Multibend fault-bend folding. Journal of Structural Geology 19, 279–292.

Mitra, S., 1990. Fault-propagation folds: geometry kinematic evolution, and hydrocarbon traps. Bulletin of the America Association of Petroleum Geologists 74, 921–945.

Morgan, J.K., Karig, D.E., 1995. Kinematics and balanced cross-section across the toe of the eastern Nankai accretionary prism. Journal of Structural Geology 17, 31–45.

Norris, D.K., 1961. An interstratal peel on Maverick Hill, Alberta. Journal of the Alberta Society of Petroleum Geologist 9, 177–191.

Pieri, P., Sabato, L., Loiacono, F., Marino, M., 1994. Il bacino di piggy-back di Sant'Arcangelo: evoluzione tettonico-sedimentaria. Bollettino Società Geologica Italiana 113, 465–481.

Poblet, J., McClay, K., 1996. Geometry and kinematics of single layer detachment folds. American Association of Petroleum Geologists Bulletin 80, 1085–1109.

Poblet, J., McClay, K., Storti, F., Munoz, J.A., 1997. Geometry of syntectonic sediment associated with single-layer detachment folds. Journal of Structural Geology 19, 369–381.

Price, R.A., 1965. Flathead map area, British Columbia and Alberta. Geological Survey of Canada Memoir 336, 221pp.

Rafini, S., Mercier, E., 2002. Forward modelling of foreland basin progressive unconformities. Sedimentary Geology 146, 75–89.

Ramsay, J.G., 1974. Development of chevron folds. Geological Society of America Bulletin 85, 1741–1754.

Rich, J.L., 1934. Mechanics of low-angle overthrust faulting as illustrated by the Cumberland Thrust Block, Virginia, Kentucky and Tennessee. American Association of Petroleum Geologists Bulletin 18, 1584–1596.

Salvini, F., Storti, F., 2001. The distribution of deformation in parallel fault-related folds with migrating axial surfaces: comparison between fault-propagation and fault-bend folding. Journal of Structural Geology 23, 25–32.

Salvini F., Storti F., 2004. Active hinge folding-related deformation and its role in hydrocarbon exploration and development: insights from HCA modeling. In: McClay, K.R. (Ed.), Thrust Tectonics and Petroleum Systems. American Association of Petroleum Geologists Memoirs, in press.

Salvini, F., Storti, F., McClay, K., 2001. Self determining numerical modelling of compressional fault-bend folding. Geology 29, 839–842.

Soto, R., Casas, A.M., Storti, F., Faccenna, C., 2002. Role of lateral thickness variations on the development of oblique structures at the Western end of the South Pyrenean Central Unit. Tectonophysics 350, 215–235.

Srivastava, D.C., Engelder, T., 1990. Crack-propagation sequence and pore-fluid conditions during fault-bend folding in the Appalachian Valley and Ridge, central Pennsylvania. Geological Society of America Bulletin 102, 116–128.

Storti, F., Poblet, J., 1997. Growth stratal architectures associated to decollement folds and fault-propagation folds. Inferences on fold kinematics. Tectonophysics 282, 353–373.

Storti, F., Salvini, F., 1996. Progressive rollover fault-propagation folding: a possible kinematic mechanism to generate regional-scale recumbent folds in shallow foreland belts. American Association of Petroleum Geologists Bulletin 80, 174–193.

Suppe, J., 1983. Geometry and kinematics of fault-bend folding. American Journal of Sciences 283, 684–721.

Suppe, J., 1985. Principles of Structural Geology. Prentice-Hall, Englwood Cliffs, NJ. 537pp.

Suppe, J., Medwedeff, D.A., 1990. Geometry and kinematics of fault-propagation folding. Eclogae Geologicae Helvetiae 83, 409–454.

Suppe, J., Chou, G.T., Hook, S.C., 1992. Rates of folding and faulting determined from growth strata, in: McClay, K.R. (Ed.), Thrust Tectonics. Chapman and Hall, London, pp. 105–121.

Woodward, N.B., 1999. Competitive macroscopic deformation processes. Journal of Structural Geology 21, 1209–1218.

Woodward, N.B., Boyer, S.E., Suppe, J., 1989. Balanced Geological Cross-section: An Essential Technique in Geological Research and Exploration. American Geophysical Union Short Course in Geology 6.